https://doi.org/10.5194/jecats-2026-12
Preprint. Discussion started: 28 July 2026

A multi-physics Eulerian framework for long-term contrail evolution (MultiCon): Single plume analysis

Amin Jafarimoghaddam[1] and Manuel Soler[1]

[1]Department of Aerospace Engineering, Universidad Carlos III de Madrid, Avenida de la Universidad 30, Leganés, 28911 Madrid, Spain

Correspondence: Amin Jafarimoghaddam (ajafarim@pa.uc3m.es)

ABSTRACT

Condensation trails (contrails) evolve from formation and rapid growth to dissipation or transition into cirrus clouds (i.e., the long-term diffusion regime), where the latter phase largely determines their radiative forcing. This research develops a high-speed Eulerian contrail plume solver for large-scale analyses while approximating the multi-physical processes governing plume evolution. We propose a unified Eulerian framework for the long-term regime of contrails that integrates the population balance equation with ice-particle growth dynamics. Under suitable assumptions, the governing nonlinear field equations admit dimensional separability, allowing the horizontal and vertical evolution to be nearly decoupled. Consequently, the plume microphysics is described by a highly nonlinear system of ((z,t)) partial differential equations (PDEs), while the horizontal evolution governs plume spreading. Since this work considers single-plume analysis, we focus mainly on the coupled vertical PDE system, extending existing large-scale contrail models from tracking bulk quantities to resolving the plume's spatiotemporal evolution. The PDEs incorporate several underexplored factors, including multiphase behavior of the bulk settling velocity of ice particles in turbulent flows, a parameterization of ice-crystal habit dynamics that modifies growth, sublimation, and settling, as well as stochastic diffusion and vertical wind. The model also introduces adjustable parameters that can be calibrated using ground-truth data to optimize the nonlinear PDEs. Owing to its computational speed (roughly below 1 second to simulate 10 hours of plume evolution), the solver is well suited for large-scale simulations of contrail evolution and radiative forcing. Notably, although the mathematical framework is general capable of resolving/approximating polydispersity, the current solver assumes a monodisperse distribution.

1 Introduction

Contrails, visible ice-crystal clouds generated by aircraft engine exhaust, are now considered to be one of the leading anthropogenic contributors to radiative forcing, with a warming effect at least comparable to that of CO_2 emissions, albeit with a high level of uncertainty Engberg et al. (2025). After rapid nucleation process and initial growth phase,

https://doi.org/10.5194/jecats-2026-12
Preprint. Discussion started: 28 July 2026

contrails may persist for hours, undergoing complex interactions between ambient winds, turbulent mixing, and microphysical growth processes before dissipating or transitioning into cirrus clouds. Capturing these evolution stages is essential for accurate estimation of contrail-induced climate impacts and for the development of mitigation strategies. Contrail modeling approaches typically fall into the following categories: (i) high-resolution simulations of individual contrails; (ii) Lagrangian plume models that follow contrail segments with prescribed microphysics; and (iii) parameterized schemes in global models Paoli and Shariff (2016).

Although contrail dynamics have been the subject of extensive research, no existing numerical framework has yet demonstrated sufficient accuracy to reproduce contrail evolution over climatological timescales, nor to rigorously quantify the associated radiative forcing Akhtar Martinez and Jarrett (2024). Most existing models lack experimental validation and often rely on oversimplified macro- and micro-scale physics. Combined with limitations in the computational framework, this has led to inconsistent results across current contrail models Akhtar Martínez et al. (2025).

In high-fidelity contrail modeling, both Reynolds-Averaged Navier–Stokes (RANS) and Large Eddy Simulation (LES) frameworks are used to resolve the jet and near-wake stages of an individual contrail plume, as well as its long-term evolution. For example, Unterstrasser et al. have conducted key LES studies on the transition from young contrails to persistent contrail cirrus, including parametric analyses of contrail evolution Unterstrasser and Gierens (2010a, b) and comparisons with natural cirrus, focusing on local-scale interactions Unterstrasser et al. (2017a, b). Their work links small-scale contrail microphysics to larger-scale cirrus dynamics, emphasizing factors that control contrail lifetime and climate impact (interested readers are referred to Guignery et al. (2012); Montreuil et al. (2018); Lewellen (2020); Bouhafid et al. (2024); Lewellen et al. (2014) for detailed high-fidelity studies of contrail formation and early plume evolution). These high-fidelity contrail models are mostly designed to simulate the temporal evolution of an individual contrail plume under idealized or synthetic environmental conditions. These models, however, are computationally intensive and therefore impractical for large-scale analyses that must represent many flights across extensive geographical domains.

To overcome this limitation, several low- and intermediate-fidelity models and parameterization schemes have been developed in the literature to reduce computational expense while preserving some physical processes governing contrail formation and evolution. Two notable examples are the Contrail Cirrus Prediction model (CoCiP) Schumann (2012) and the Aircraft Plume Chemistry, Emissions, and Microphysics Model (APCEMM) Fritz et al. (2020), both widely used in the aviation community.

CoCiP (Schumann (2012)) represents the long-term evolution of contrails using a Lagrangian Gaussian–plume framework in which bulk scalar quantities (e.g., ice-water content and related moments) evolve according to prognostic ordinary differential equations and are advected with the flow. The three-dimensional contrail geometry is reconstructed diagnostically from these scalar fields using Gaussian kernels, such that spatial structure is parameterized rather than explicitly resolved. Consequently, CoCiP implements a bulk (effectively zero-dimensional in particle size and in-cloud microstructural space) microphysical description: ice microphysics are represented by two prognostic bulk variables —

https://doi.org/10.5194/jecats-2026-12
Preprint. Discussion started: 28 July 2026

the total ice mass and the total number of ice crystals (commonly treated as monodisperse) — and contrail formation and subsequent growth/sublimation are constrained by the Schmidt–Appleman criterion Schumann et al. (1995); Gierens et al. (2003); Seinfeld and Pandis (2016). Physical processes operating at sub-plume scales (e.g., wind-shear, and turbulent diffusion) are parameterized in the plume spreading and mixing schemes rather than being resolved explicitly. Although CoCiP is suited for large-scale, long-term simulations, it omits several key processes, such as coupling of advection and diffusion in spatiotemporally varying wind fields; interactions between co-existing plumes in single-flight assessments; explicit along-track dispersion; and a prognostic, polydisperse size spectrum (or grid-based sensitivity to the monodisperse assumption). Its parameterization of short-term contrail development prior to the diffusion regime is also limited, lacking detailed chemistry, aerosol interactions beyond ice mass, and ice nucleation dynamics. Similar limitations apply to the Ames Contrail Simulation Model (ACSM) (Li et al. (2023)), which is based on nearly the same theoretical framework as CoCiP.

APCEMM (Fritz et al. (2020)) is a Lagrangian plume-scaling model that explicitly simulates the two-dimensional cross-sectional evolution of aircraft exhaust plumes. It applies the Schmidt–Appleman criterion to determine contrail formation and subsequently models the evolution of vapor and particles through detailed microphysics and chemistry. APCEMM utilizes binned (sectional) aerosol and ice microphysics alongside two-dimensional advection and diffusion processes to capture the contrail cross-section dynamics. The model also incorporates a unified chemical mechanism encompassing both gas-phase and heterogeneous reactions, accounting for exhaust species such as NO_x and soot, and their influence on plume behavior. Contrail ice naturally forms in the simulation once water vapor supersaturates on soot particles; thereafter, the ice is transported and dispersed by ambient wind shear and gravitational settling. Compared to CoCiP, APCEMM is more computationally intensive, and in practice, it typically predicts longer contrail lifetimes and stronger radiative forcing than CoCiP under similar conditions Xu et al. (2023); Xu (2024). While APCEMM advances contrail representation, it still shares some of CoCiP's limitations in the long-term diffusion regime, such as the coupling of advection and diffusion in spatiotemporally varying wind fields, and interactions between coexisting plumes during single-flight assessments.

Nonetheless, and besides the limitations described above, neither CoCiP nor APCEMM incorporate two microphysical processes that are relevant in the long-term contrail evolution: 1) habit development and 2) bulk settling velocity of ice particles.

When it comes to habit development, it is well known that persistent contrails and contrail cirrus are dominated by faceted, non-spherical ice crystals that closely resemble those in natural cirrus clouds. Both in situ observations and remote sensing studies consistently demonstrate that contrail ice particles deviate from spherical shapes. For instance, Yang et al. (2010) report that contrails and contrail-cirrus clouds are composed almost exclusively of nonspherical ice crystals. Polarimetric lidar measurements further support this by revealing strong light depolarization signals indicative of non-spherical particles. Similarly, CALIPSO satellite retrievals confirm that non-spherical ice dominates persistent contrails IPCC (1999). Iwabuchi et al. (2012) find that depolarization ratios measured in contrails align well with theoretical predictions for mixtures of randomly oriented, nonspherical ice habits. As contrails age and spread,

https://doi.org/10.5194/jecats-2026-12
Preprint. Discussion started: 28 July 2026

larger faceted crystals, including plates, columns, and rosettes, become increasingly prevalent. Complex crystal shapes such as irregular bullet rosettes have also been observed. Concurrently, the effective radii of ice crystals increase with contrail age. Recent reviews indicate that, in older contrails (age > 120 s), most ice crystals have effective radii ranging from 10 to 150 μm Krämer et al. (2020); Wolf et al. (2023). Field campaigns have also documented crystals reaching several hundred microns in size Iwabuchi et al. (2012). Specifically, once contrail ice crystals exceed a critical size (typically around $5-10\mu$m diameter), they experience microphysical behaviors analogous to those in natural cirrus clouds. Empirical evidence from in situ sampling at approximately $-61°$C shows that contrail ice crystals with effective radii larger than about 10 μm predominantly exhibit habits characteristic of natural cirrus: roughly 75% hexagonal plates, 20% columns, and a smaller fraction of triangular plates. These habits emerge irrespective of the initial nucleation mechanism. Therefore, mature contrail cirrus transition into the same microphysical regime as natural cirrus, where habit classification based on temperature and supersaturation is appropriate Yang et al. (2010). However, the dominant ice crystal habits and their variation with contrail age and crystal size remain poorly understood Kärcher (2018).

The bulk settling velocity of ice particles is also a relevant microphysical process in long-term contrail evolution. The terminal velocity of an isolated, spherical particle (e.g. as estimated from Stokes' law) is often used in long-term contrail models such as in COCIP and APCEMM, but it does not capture collective, multiphase effects that determine the effective downward speed of an ensemble of crystals, particularly for contrail models that neglect explicit fluid–solid coupling. The *bulk* settling velocity denotes the ensemble-averaged settling behaviour of particles embedded in a carrier fluid and thus inherently reflects particle–fluid and particle–particle interactions as well as turbulence modulation. Multiphase simulations and laboratory experiments routinely document substantial departures of ensemble settling from single-particle terminal velocities Stout et al. (1995); Chen et al. (2020); Akutina et al. (2020); Fornari et al. (2016), driven by processes such as *loitering*, and *preferential sweeping*.

In this research, we present a unified Eulerian framework for contrail evolution that rigorously couples macro- and microphysical processes within a single computational domain. The framework resolves three-dimensional spatiotemporal interactions of contrail plumes for single-flight assessments and scales efficiently to large-scale scenarios with low computational cost. Macro-scale dynamics are described by moment equations derived from the Population Balance Equation (PBE) (Ramkrishna (2000)). Microphysics (involving growth kinetics of individual ice crystals) are represented by Eulerian field equations. These microphysical fields are further coupled to a habit-dynamics field equation that solves shape-evolution, enabling a continuous representation of ice-crystal geometry throughout the contrail life cycle. Within this framework, we distinguish the particle-scale terminal velocity (function of crystal mass and projected area-known as Stokes formula) from the ensemble-scale bulk settling velocity. By performing an analysis of the multi-phase flow equations under high turbulent mixing, we derive a first-order Burgers'-type equation that accounts for the collective bulk settling velocity. In addition, we demonstrate that, under mild assumptions, the governing equations exhibit separability, making the model particularly well-suited for large-scale simulations with a favorable balance between accuracy and computational cost.

https://doi.org/10.5194/jecats-2026-12
Preprint. Discussion started: 28 July 2026

Notably, although the presented Eulerian framework is general, the corresponding micro- and macro-scale field equations are derived primarily under the assumption of monodispersity for simulation purposes. Extension to polydispersity is straightforward and reserved for future studies. However, because the main focus of the present work is to introduce the framework itself, the simulations reported here employ the minimal (monodisperse) representation of the Eulerian framework, focusing on single-plume evolution.

2 Modeling Framework for Long-Term Contrail Evolution

Two primary modeling frameworks can be employed to study the formation and persistence of aircraft contrails. In the Lagrangian framework, particles are followed along their trajectories and the governing dynamics are applied along each path. By contrast, the Eulerian approach describes the evolution of particle-size (or mass) distributions via the Population Balance Equation (PBE) (Breit et al. (2025)), often cast as a coupled system of advection–diffusion equations (ADE) with suitable closure assumptions (e.g. Pruppacher and Klett (1997)). In this study, we focus on the **long-term evolution** regime (after the jet-induced wake has decayed) and introduce a novel Eulerian formulation that conserves both particle number and mass by retaining the zeroth and first moments of the PBE.

Stages of Contrail Evolution. Contrail development progresses through three to four overlapping regimes (Paoli and Shariff (2016)).

1. **Jet/vortex-regime (vortex roll-up) and nucleation (seconds):** Immediately downstream of the engine exit, extremely high supersaturations drive rapid homogeneous or heterogeneous nucleation of very small ice crystals. Hydrodynamic shear and coherent vortex structures dominate their dispersion and early collision/coalescence behavior.

2. **Intermediate vortex wake descent/break up (minutes):** As the strong jet vortices break down, crystals remain small and are mixed by decaying turbulent eddies. Temperature and humidity start to relax toward ambient values, but settling effects are still minor compared to turbulent mixing.

3. **Long-term diffusion and habit development (tens of minutes to hours):** Once the jet-induced turbulence has dissipated, only the ambient wind and residual turbulence remain. In this regime, two competing inertial-turbulence mechanisms, loitering (enhanced drag from small-eddy sampling slows settling) and preferential sweeping (partial decoupling drives larger crystals into downward-moving regions), govern the net particle descent. Notably, the net radiative forcing attributable to contrails is overwhelmingly determined during this long-term, contrail-cirrus stage.

The MultiCon model is designed to simulate the long-term diffusion and habit-evolution regime by coupling the ice-particle velocity (comprising the ambient wind and turbulence-modified settling velocity) with the governing microphysical source terms and diffusion closures. After invoking a separability ansatz, the governing equations reduce to a set of coupled nonlinear PDEs, which are described in detail in Sec. 5. The initial conditions for these PDEs are naturally supplied by the preceding jet and vortex regimes of contrail evolution. To demonstrate the range of plume topologies that the model can represent, we initialize the PDE system using physically representative values of the

https://doi.org/10.5194/jecats-2026-12
Preprint. Discussion started: 28 July 2026

line-number concentration, initial ice crystal radius, and the initial horizontal and vertical standard deviations of the contrail plume. The initialization procedure is also described in Sec. 5. For the comparison with CoCiP presented in Sec. 6.1, however, we adopt the same parameterization of the jet and vortex regimes as implemented in CoCiP to ensure a consistent comparison between the two models.

2.1 Modeling Assumptions

The development of the present model relies on the following assumptions.

First, post-formation nucleation is considered negligible. Following the initial rapid nucleation phase during contrail formation, no significant subsequent nucleation events are assumed to occur. As a result, the ice-particle number concentration remains conserved in the absence of external source/sink terms such as aggregation process (Pruppacher and Klett (1997)).

Second, we assume the dominance of ambient wind-driven advection. Transient aerodynamic effects, such as wake vortices and aircraft-induced jets, are regarded as short-term phenomena. Consequently, the long-term advection of contrail particles is driven primarily by the ambient wind field and the gravitational settling velocity of the particles.

Third, we adopt a spheroidal approximation for ice-particle geometry. This approach, consistent with the modeling framework of Chen and Lamb (1994), and Nelson and Baker (1996) allows the treatment of complex hexagonal habits as spheroids, thereby generalizing the mathematical representation of growth and settling dynamics.

Finally, each computational cell is characterized by an average ice-particle mass, number concentration, mass concentration, and shape index, thereby assuming a locally monodisperse particle distribution through the use of the Kronecker delta function in the PBE. Nevertheless, the grid dependency of the plume in the sensitive vertical dimension has been assessed, and a fine mesh resolution was selected at which the field equations were convergent.

2.2 Multiphysics Modeling Building Blocks

Fig. 1 elucidates the flow of this study focusing on the primary building blocks of the MultiCon model (monodisperse version) to resolve the long-term evolution of contrails.

To elaborate, we begin by deriving the monodisperse equation from the PBE in **Sec.** 3, with detailed steps provided in **Appendix** A. The formulation further requires the derivation of key components, including the bulk settling velocity (presented in **Sec.** 4 and detailed in **Appendices** B, and C), growth and sublimation microphysics (detailed in **Appendix** F), and habit dynamics (detailed in **Appendix** E). To close the system of PDEs, an additional equation describing the water vapor balance is introduced in **Sec.** 5, while the corresponding derivations and detailed explanations are presented in **Appendix** G.

In summary, the governing system of PDEs solves for four variables: number concentration, mass concentration, ice crystal habit, and supersaturation, which are strongly coupled through settling velocity, growth/sublimation rates, and habit-change rate.

https://doi.org/10.5194/jecats-2026-12
Preprint. Discussion started: 28 July 2026

JECATS DISCUSSIONS

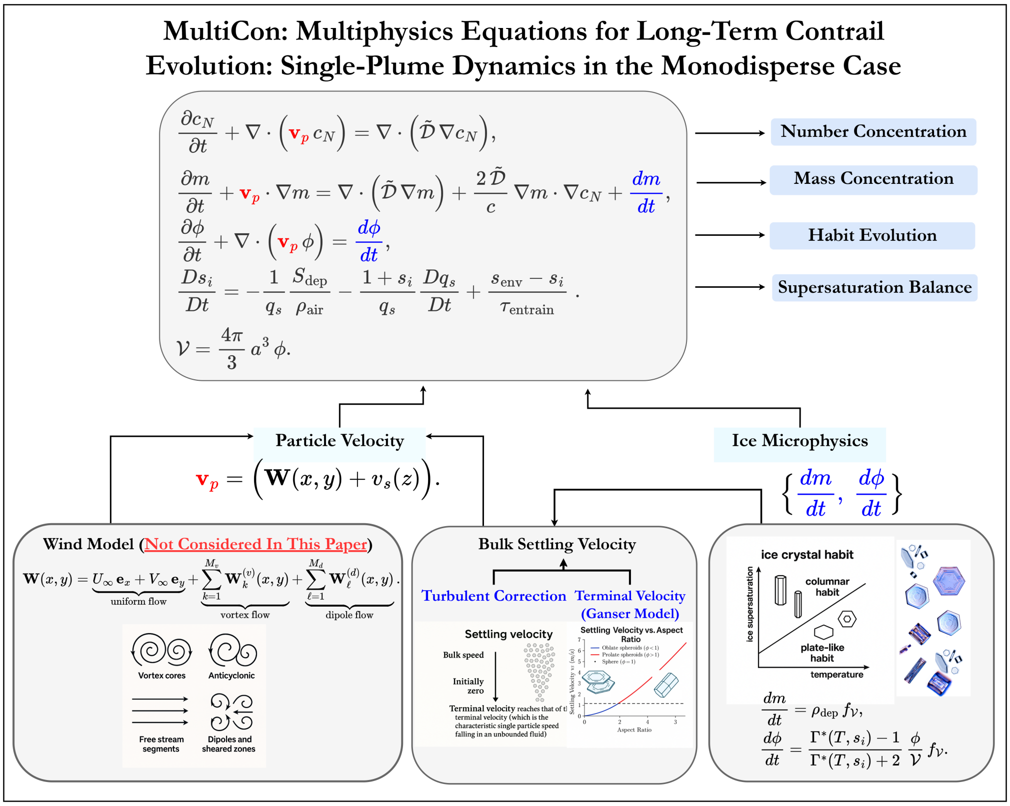

Figure 1. Schematic diagram showing the flow of this study focusing on the primary building blocks of the MultiCon model

3 Multi-Physics Monodisperse Equations for Long-Term Contrail Evolution

3.1 Governing Equations for Bulk Motion

Based on the above assumptions, we begin modeling the evolution of persistent contrails by the following system of coupled advection–diffusion equations (see Appendix A):

$$
\begin{aligned}
&\frac{\partial c_N}{\partial t} + \nabla\cdot\left(\mathbf{v}_p\, c_N\right) = \nabla\cdot\left(\tilde{\mathcal{D}}\,\nabla c_N\right) + S_{c_N},\\
&\frac{\partial c_M}{\partial t} + \nabla\cdot\left(\mathbf{v}_p\, c_M\right) = \nabla\cdot\left(\tilde{\mathcal{D}}\,\nabla c_M\right) + c_N\,\rho_{\mathrm{dep}}\, f_{\mathcal{V}} + S_{c_M}.
\end{aligned}
\tag{1}
$$

In the equations above, t is time, $\mathbf{x} := (x, y, z)$ is the system coordinate in a Cartesian framework, $c_N := c_N(\mathbf{x}, t)$ and $c_M := c_M(\mathbf{x}, t)$ represent the ice-particle number and mass concentrations, respectively. The bulk velocity of the ice particles is given by $\mathbf{v}_p := \mathbf{v}_p(\mathbf{x}, t)$, and the nonlinear stochastic isotropic diffusion coefficient matrix is denoted by $\tilde{\mathcal{D}}$. Moreover, $S_{c_N} := S_{c_N}(\mathbf{x}, t)$ and $S_{c_M} := S_{c_M}(\mathbf{x}, t)$ represent the source terms for the ice-particle number and mass

https://doi.org/10.5194/jecats-2026-12
Preprint. Discussion started: 28 July 2026

concentrations, respectively, due to additional release of ice particles. In the present study the source/sink term is neglected (i.e., $S_c = 0$). However, for large-scale simulations, the term S_c may be included in the governing transport equations to account for additional release of ice particles. Alternatively, for large-scale simulations, one may set $S_c = 0$ and adjust the initial conditions to represent a continuous release of ice particles. Finally, $f_\mathcal{V} := f_\mathcal{V}(a, \phi, \mathbf{x}, t)$ represents the volumetric growth rate of individual particles, ρ_{dep} denotes the effective deposition density, where a is the ice particle's equatorial radius and ϕ is the ice-particle shape index, which will be elaborated in the next section.

3.2 Governing Equations for Individual Ice Particles' Dynamics

Modeling persistent contrails also requires microphysical equations that describe the evolution of individual ice particles' mass and shape. Accurate parameterization of contrail single-scattering properties, and thus reliable simulation of contrail and contrail-cirrus radiative forcing, requires explicit representation of the crystal nonsphericity (Yang et al. (2010)). Employing the habit dynamic framework by Chen and Lamb (1994), and Nelson and Baker (1996), the coupled ODEs describing the evolution of ice crystal mass and shape can be written as:

$$\frac{dm}{dt} = \rho_{\text{dep}}\, f_\mathcal{V}(a, \phi, \mathbf{x}, t), \qquad \frac{d\phi}{d\mathcal{V}} = \frac{\Gamma^*(T, s_i) - 1}{\Gamma^*(T, s_i) + 2}\,\frac{\phi}{\mathcal{V}}, \qquad \mathcal{V} = \frac{4\pi}{3}\, a^3\, \phi. \tag{2}$$

In the above, m is the individual ice particle mass, $\mathcal{V}$ corresponds to the volume of an individual ice particle, while ϕ represents the individual ice-particle shape index, defined as $\phi := \frac{c}{a}$, where a is the equatorial radius and c is the transverse radius; $\phi > 1$ indicates columnar (prolate) crystals and $\phi < 1$ denotes plate-like (oblate) crystals. $T := T(\mathbf{x}, t)$ is the spatiotemporal temperature field, and $s_i := s_i(\mathbf{x}, \mathbf{t})$ represents the spatiotemporal background/ambient ice supersaturation field. In addition, Γ^* is known as Inherent Growth Factor (IGF), and ($f_\mathcal{V} := f_\mathcal{V}(a, \phi, \mathbf{x}, t)$) denotes the volumetric growth rate of individual ice particles (see Appendix E, and F)[1].

For completeness, we note that laboratory evidence suggests the aspect ratio of ice crystals remains constant during sublimation. This is attributed to the uniformity of vapor density along the crystal surface, which results in shape preservation throughout the sublimation process Nelson and Knight (1998); Magee et al. (2014); Ham (1959).

Notably, the Eulerian framework requires that the mass and shape dynamics, $m(t)$ and $\phi(t)$, be reformulated as field equations $m(\mathbf{x}, t)$ and $\phi(\mathbf{x}, t)$ through additional ADEs. However, the field quantity $m(\mathbf{x}, t)$ can be obtained from the identity $c_M := m\, c_N$, implying that solving for c_M also yields $m(\mathbf{x}, t)$. Nevertheless, we provide an explicit ADE for $m(\mathbf{x}, t)$ both for completeness of the Eulerian framework and as an alternative to the ADE for c_M [2].

[1] Notably, parameterizations of ice-vapor growth exert a first-order control on cold-cloud behavior Gierens et al. (2003); Avramov and Harrington (2010). While laboratory and theoretical advances have yielded useful, approximate growth models, the detailed physical processes governing ice-crystal development remain incompletely characterized. In addition, the ice crystal quantities measured at different temperatures cannot be directly incorporated into the capacitance model, a formulation that nonetheless underlies many atmospheric ice-growth simulations (see e.g., Libbrecht (2003); Nelson and Knight (1998)). This inconsistency highlights a persistent gap between process-oriented laboratory observations and the bulk parameterization employed in large-scale atmospheric models.

[2] We also highlight that the spatial dependence of m and ϕ is significant since temperature and ice supersaturation are spatiotemporal fields, i.e., $T(\mathbf{x}, t)$, and $s_i := s_i(\mathbf{x}, \mathbf{t})$. More specifically, if one were to assume $T = T(t)$, and $s_i = s_i(t)$, then one would have $m = m(t)$ and $\phi = \phi(t)$, implying that the Eulerian framework would collapse to a Lagrangian one. Unlike the Eulerian framework (in which spatial coordinates $\mathbf{x}$ and time t serve as independent variables in PDEs) the Lagrangian approach parameterizes position as a time-dependent

https://doi.org/10.5194/jecats-2026-12
Preprint. Discussion started: 28 July 2026

3.3 Eulerian Framework for Single-Plume Evolution

As discussed, we can obtain an ADE accounting for the evolution the mass field $m(\mathbf{x},t)$ directly (see the derivation details in Appendix A)[3]. However, it is not possible to directly formulate an ADE for particle shape evolution in the same sense as for mass concentration. Although a particle entering a control volume transports both its mass and specific shape, only mass is a conserved scalar obeying continuity laws. In contrast, particle shape evolves through micro-physical processes that fundamentally differ from diffusion. Therefore, in the Eulerian framework for particle shape evolution, only an advection term is incorporated to ensure the presence of the shape index $\phi(\mathbf{x},t)$ in all regions where particles are present, followed by a term describing its micro-physical evolution that determines the rate at which particle shapes change. Therefore, the Eulerian equations governing the long-term evolution of contrails are presented as:

$$
\begin{aligned}
&\frac{\partial c_N}{\partial t} + \nabla \cdot \left(\mathbf{v}_p c_N\right) = \nabla \cdot \left(\tilde{\mathcal{D}}\nabla c_N\right),\\
&\frac{\partial m}{\partial t} + \mathbf{v}_p \cdot \nabla m = \nabla \cdot \left(\tilde{\mathcal{D}}\nabla m\right) + \frac{2\tilde{\mathcal{D}}}{c}\nabla m \cdot \nabla c_N + \rho_{\text{dep}}\, f_{\mathcal{V}},\\
&\frac{\partial \phi}{\partial t} + \nabla \cdot \left(\mathbf{v}_p \phi\right) = \frac{\Gamma^*(T,s_i)-1}{\Gamma^*(T,s_i)+2}\,\frac{\phi}{\mathcal{V}}\, f_{\mathcal{V}}, \quad \mathcal{V} = \frac{4\pi}{3}a^3\phi
\end{aligned}
\tag{3}
$$

Mathematically, closing the governing system requires an additional PDE to account for the spatiotemporal evolution of the background supersaturation, as detailed in Sec. 5.

In the following section, we present the theory and formulas for the remaining building block of the Eulerian model, which includes the ice particle velocity $\mathbf{v}_p$.

4 Ice Particle Velocity $\mathbf{v}_p$

The total ice-particle bulk velocity field $\mathbf{v}_p(\mathbf{x},t)$ is defined as:

$$
\mathbf{v}_p = \mathbf{v}_{slp} + \underbrace{(w_x,w_y,w_z)^\top}_{\substack{\text{background velocity}\\ \text{(wind components)}}} \approx (0,0,v_s)^\top + \underbrace{(w_x,w_y,w_z)^\top}_{\text{background velocity}} = (w_x,w_y,w_z+v_s)^\top. \tag{4}
$$

In Eq. (A2), $\mathbf{v}_{slp}$ represents the bulk slip velocity of the particle phase within a turbulently mixing fluid, while v_s denotes the bulk settling velocity. In the subsequent section, we develop a new model for v_s derived from a

trajectory $\mathbf{x}(t)$, leaving time as the sole independent variable. Consequently, the governing transport physics reduces to a system of ODEs that solve for bulk quantities (as in CoCiP) without explicitly resolving internal spatial gradients. Mathematically, even when a single plume is discretized into multiple sub-regions tracked by individual trajectories $\mathbf{x}_i(t)$, this formulation fails to rigorously capture the localized, non-linear coupling between advection and diffusion terms.

[3]It is noteworthy that the equation governing $m(\mathbf{x},t)$ can also be derived directly from the quotient rule $c_M := m c_N$ by defining the net inlet flux into the control volume as $\mathbf{J}_{in} := m(\mathbf{x},t)c_N(\mathbf{x},t)$, and the net outlet flux expressed as $\mathbf{J}_{out} = \mathbf{J}_{in} + \frac{\partial}{\partial \mathbf{x}_i}\mathbf{J}_{in}$. The derivation is accomplished on using the conservation of the number concentration as the closure equation.

https://doi.org/10.5194/jecats-2026-12
Preprint. Discussion started: 28 July 2026

rigorous analysis and reduction of the multiphase flow equations, incorporating an Euler–Euler framework for interphase momentum exchange and particle transport. Given that the mean vertical wind component w_z is negligible, subgrid-scale vertical fluctuations can be embedded into the definition of v_s.

4.1 Bulk Settling Velocity v_s: A Low-Order Theoretical Model

Traditional approaches to particle settling rely on the terminal velocity derived for individual particles in unbounded domain using Stokes' law. However, in an Eulerian framework that describes the bulk concentration of particles (such as ice particles in contrails), the settling velocity must reflect the collective behavior of particles that are also subject to turbulent mixing[4]. In high-altitude regions, significant turbulent mixing implies that the ice particles initially 'hover' within the eddy-viscous layer while undergoing growth (provided that the growth conditions are met). This motivates a model in which the effective settling velocity is determined not only by gravitational and drag forces but also by turbulent (or self-) diffusion. To differentiate notations, we use $v_\mathbf{s}$ for the particle effective/bulk settling velocity and $v_\mathbf{ter}$ for the terminal settling velocity, typically derived from Stokes' law (or alternative empirical formulas) for a single settling particle in an unbounded domain.

In turbulent flows, small particles can experience a phenomenon known as *loitering*. Due to their ability to be readily carried by rapidly fluctuating eddies (sometimes referred to as the eddy-locking, analogous to behavior seen in nanofluids Buongiorno (2006); Jafarimoghaddam et al. (2021)), these particles sample a broad range of flow directions and, as a consequence, effectively experience enhanced nonlinear drag and may follow a longer trajectory to settle across a given vertical distance. This results in an average fall speed that is reduced relative to predictions based on quiescent conditions. A second mechanism, commonly referred to as *preferential sweeping*, occurs when particles possess sufficient inertia to partially decouple from the turbulent eddies. They are centrifuged out of vortical cores and thus become concentrated in downward-moving regions of the flow, causing them to sample stronger downward velocity fluctuations and hence to acquire an enhanced mean settling velocity. The relative influence of these two mechanisms depends on the degree to which the particles are able to track turbulent fluctuations. Very small crystals tend to follow the turbulence closely, resulting in persistent agitation and reduced descent rates due to the *loitering* effect. *Preferential sweeping* becomes significant when particles grow large enough, or turbulence weakens sufficiently, to allow them to slip out of the smallest vortices. In the specific case of contrail cirrus, where ice crystals remain very small under considerable atmospheric turbulence, the *loitering* mechanism is expected to dominate the early stages of evolution. Over time, as the particles grow by nearly an order of magnitude, they are expected to begin *sweeping* toward their terminal velocity (or even exceed it) typically when their Stokes number reaches $St = \mathcal{O}(1)$ or their Galileo number reaches $Ga = \mathcal{O}(10^2–10^3)$, both of which are characteristic of larger particles (typically with radii greater than $50 - 100\,\mu$m) (interested readers are referred to Stout et al. (1995); Chen et al. (2020); Akutina et al. (2020); Fornari et al. (2016); Kaveh and Malcherek (2024)).

[4] The same comment applies to contrail models formulated within a Lagrangian framework without coupling to the surrounding fluid phase.

https://doi.org/10.5194/jecats-2026-12
Preprint. Discussion started: 28 July 2026

In this section, we develop a low-order theoretical model that captures these effects; specifically, the initial *loitering* behavior decays asymptotically into *preferential sweeping*, thereby recovering the terminal velocity.

In turbulent flows, particularly under quasi-isotropic conditions, it is reasonable to assume that the turbulent diffusivity and the eddy viscosity are related by a turbulent Schmidt number, Sc_t, such that: $\tilde{\mathcal{D}} \approx \frac{\nu_t}{Sc_t}$. For many atmospheric and geophysical flows, the turbulent Schmidt number is of order unity. In our formulation, we adopt an effective turbulent viscosity $\nu_{\mathbf{t,ef}}$ that represents the 3D-averaged mixing. This is justified by the fact that the overall turbulent mixing experienced by the particles is inherently three-dimensional. Thus, we write: $\nu_{\mathbf{t,ef}} \approx \langle \tilde{\mathcal{D}}_{(x,y,z)} \rangle$, accounting for the total mixing of the particle-laden flow. The directional diffusivities $\tilde{\mathcal{D}}_x, \tilde{\mathcal{D}}_y, \tilde{\mathcal{D}}_z$ vary with ambient turbulence and stratification; for far-wake, cruise-altitude contrails we adopt $\tilde{\mathcal{D}}_x = \tilde{\mathcal{D}}_y \in [10, 40]\ \mathrm{m^2\,s^{-1}}$, and $\tilde{\mathcal{D}}_z \in [0.05, 0.50]\ \mathrm{m^2\,s^{-1}}$ giving the arithmetic mean $\nu_{\mathbf{t},\mathrm{ef}} \in [6.68, 26.83]\ \mathrm{m^2\,s^{-1}}$.

Beginning with the Euler-Euler framework for multiphase flows, where fluid and particulate phases are interpreted as continua, the momentum equation for the particle phase can be written as (see Appendix B):

$$\frac{\partial \mathbf{v}_{\mathrm{slp}}}{\partial t} + (\mathbf{v}_{\mathrm{slp}} \cdot \nabla)\mathbf{v}_{\mathrm{slp}} = \nu_t \nabla^2 \mathbf{v}_{\mathrm{slp}} + \boldsymbol{C}_f + \boldsymbol{C}_{c_M, c_N, f_{\mathcal{V}}}. \tag{5}$$

where $\boldsymbol{C}_f$ represents the coupling between $\mathbf{v}_{\mathrm{slp}}$ and the fluid phase, and is expressed as $\boldsymbol{C}_f = -\frac{\nabla p}{\rho_p} + \mathbf{g} + \frac{f_d}{\rho_p}$; and $\boldsymbol{C}_{c_M, c_N, f_{\mathcal{V}}}$ captures the coupling of $\mathbf{v}_{\mathrm{slp}}$ to the mass and number concentration fields, as well as to the growth term, and is given by $\boldsymbol{C}_{c_M, c_N, f_{\mathcal{V}}} = -\frac{\mathbf{v}_{\mathrm{slp}}}{\epsilon_p}\left[\nabla \cdot \left(\tilde{\mathcal{D}} \nabla \epsilon_p\right) + f_{\mathcal{V}}\left(\bar{m}(\mathbf{x},t), \mathbf{x}, t\right) c_N(\mathbf{x},t)\right] + \nu_t \left[\frac{1}{\epsilon_p}(\nabla \epsilon_p \cdot \nabla)\mathbf{v}_{\mathrm{slp}} + \frac{1}{\epsilon_p}(\nabla \epsilon_p \cdot \nabla)^\top \mathbf{v}_{\mathrm{slp}}\right]$.

Therefore, as detailed in (Appendix B), fully resolving the particle momentum equation requires additional closures for the fluid phase, as well as for f_d, which represents the average drag force experienced by individual particles, distinct from the drag force on a single settling particle in an unbounded domain, and also depends critically on the specification of appropriate boundary and initial conditions.

The present model assumes that particles are taken to be initially at rest on a reference plane $z_{\mathbf{ref}}$, where the concentration is highest, and that they are entrained in the turbulent flow, within which the *loitering* effect dominates. Far below $z_{\mathbf{ref}}$, after sufficient diffusion, dilution, and (for ice) growth, *loitering* becomes negligible and it is assumed that v_s *sweeps* towards the terminal velocity $v_{\mathbf{ter}}$.

Therefore, following the discussions presented in Appendix B we write the governing equation for the *low-order model*, a Burgers-type partial differential equation, together with the associated initial and asymptotic boundary conditions, as:

$$\begin{aligned} &\frac{\partial v_s}{\partial t} + v_s \frac{\partial v_s}{\partial z} = \nu_{\mathbf{t,ef}} \frac{\partial^2 v_s}{\partial z^2}, \\ &v_s(z_{\mathbf{ref}}, t=0) = 0, \qquad v_s(z \ll z_{ref}, t=0) = v_{\mathbf{ter}}, \qquad \lim_{t \to \infty} v_s(z,t) = v_{\mathbf{ter}}. \end{aligned} \tag{6}$$

https://doi.org/10.5194/jecats-2026-12
Preprint. Discussion started: 28 July 2026

We highlight that, by deliberately encoding the body force within the boundary conditions, the model circumvents the uncertainties and complexities associated with explicitly coupling the body force to the fluid phase and concentration field.

The governing equation requires a closure model to define the threshold distance beyond which turbulent mixing, characterized by the eddy viscosity $\nu_{\mathbf{t,ef}}$, effectively smooths velocity deviations over a vertical extent denoted by $z_{\mathbf{relax}}$.

To characterize $z_{\mathbf{relax}}$, we can either consider a local or global diffusion–advection balance. In *local diffusion–advection balance*, $z_{\mathbf{relax}}$ is estimated by equating vertical advection and turbulent mixing rates: $v_{\mathbf{ter}} \cdot (\Delta v_s/\delta) \sim \nu_{\mathbf{t,ef}} \cdot (\Delta v_s/\delta^2)$, which yields $\delta \equiv z_{\mathbf{relax}} \sim \nu_{\mathbf{t,ef}}/v_{\mathbf{ter}}$. However, in a *global diffusion–advection balance*, particles sample turbulent structures of size L_e as they settle; for long-term contrails L_e represents the characteristic size of dominant turbulent structures, typically 10–10^3 m. The advection time across one eddy is defined as $\tau_{\mathrm{adv}} := L_e/v_{\mathbf{ter}}$, during which turbulent diffusion spreads the velocity deviations over a distance $\delta \equiv z_{\mathbf{relax}} \sim \sqrt{\nu_{\mathbf{t,ef}} \cdot \tau_{\mathrm{adv}}} = \sqrt{\nu_{\mathbf{t,ef}} \cdot L_e/v_{\mathbf{ter}}}$. Therefore, we rewrite Eq. (6) (adapted to both the axis direction and the settling sign on defining $\hat{v}_s := |v_s|$), together with the initial condition, as:

$$\frac{\partial \hat{v}_s}{\partial t} + \hat{v}_s \frac{\partial \hat{v}_s}{\partial z} = \nu_{\mathbf{t,ef}} \frac{\partial^2 \hat{v}_s}{\partial z^2}, \quad \hat{v}_s(z,0) = \begin{cases} v_{\mathbf{ter}}, & z \leq z_{\mathbf{relax}}, \\ 0, & z > z_{\mathbf{relax}}. \end{cases} \tag{7}$$

On using the classic Cole–Hopf transformation, the final closed-form solution is obtained as (see Appendix C):

$$\hat{v}_s(z,t) = v_{\mathbf{ter}} \frac{q_0(z,t)}{q_0(z,t) + q_1(z,t)} \tag{8}$$

where:

$$q_0(z,t) = \mathrm{erfc}\left(\frac{\Delta_0 - v_{\mathbf{ter}} t}{2\sqrt{\nu_{\mathbf{t,ef}} t}}\right) \exp\left(\frac{v_{\mathbf{ter}}^2 t}{4\nu_{\mathbf{t,ef}}} - \frac{v_{\mathbf{ter}} \Delta_0}{2\nu_{\mathbf{t,ef}}}\right), \quad q_1(z,t) = \mathrm{erfc}\left(-\frac{\Delta_0}{2\sqrt{\nu_{\mathbf{t,ef}} t}}\right), \quad \Delta_0 = z - z_{\mathbf{relax}}. \tag{9}$$

As is evident, the computation of the bulk settling velocity $\hat{v}_s$ (Eq. 8) requires the determination of the terminal velocity. To this end, we consider randomly oriented spheroidal ice particles settling under gravity in a quiescent fluid and apply the drag model proposed by Ganser (1993) (see Appendix D).

4.1.1 Preliminary Results for the Bulk Settling Velocity v_s

To elucidate the bulk-settling closed-form formula, we evaluate Eq. (8) by fixing the equatorial radius at 25 μm while varying the particle shape index ϕ. Note that here, shape index ϕ and equatorial radius a are fixed in each run, resulting in fixed $v_{\mathbf{ter}}$ which is not a realistic scenario and hence, Fig. 2 only shows the behavior of the closed-form solution for the bulk settling velocity.

https://doi.org/10.5194/jecats-2026-12
Preprint. Discussion started: 28 July 2026

In particular, the plots show the variation of the settling ratio, defined as the ratio of the bulk settling velocity of the particles (accounting for loitering and preferential sweeping effects) to their individual terminal settling velocity (which neglects particle interactions with the background turbulent flow). In other words, this ratio, $v_s(z,t)/v_{\text{ter}}$, quantifies the extent to which the actual bulk settling behavior deviates from the settling behavior of isolated particles. Although the overall trend observed in Fig. 2 is qualitatively consistent with the expected effects of loitering and preferential sweeping, calibrating the empirical constants in Eq. (8) requires a more rigorous analysis and comparison with experiments that realistically reproduce atmospheric turbulence.

As shown in Fig. 2, smaller ice crystals remain suspended for longer durations due to the dominance of turbulent mixing (*loitering*) over gravitational settling (*preferential sweeping*). In contrast, for larger particles, gravitational effects rapidly outweigh turbulent dispersion, resulting in the bulk settling velocity v_s converging more quickly to the individual terminal velocity $v_{\mathbf{ter}}$.

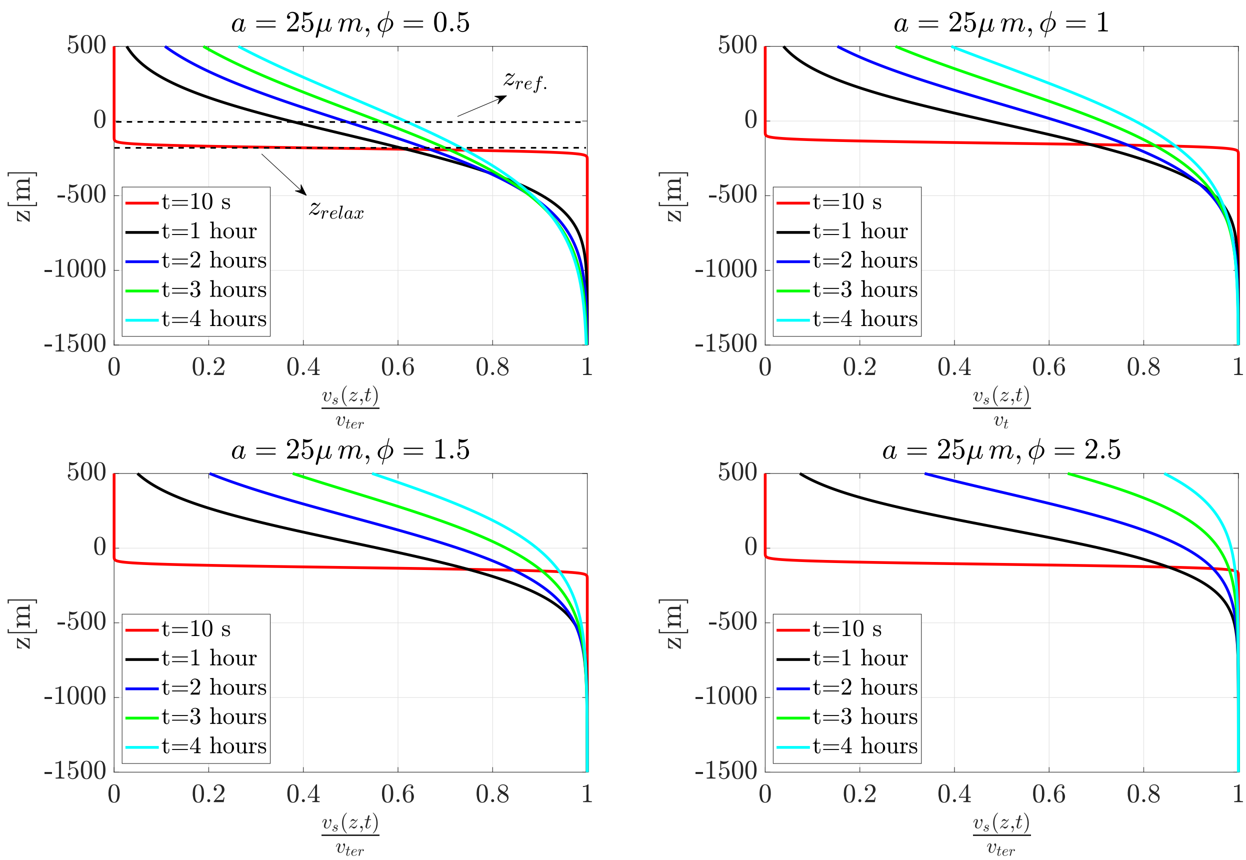

Figure 2. bulk settling velocity ratio ($\frac{v_s(z,t)}{v_{\mathbf{ter}}}$) at fixed equatorial radius $a = 25\mu m$ and varying shape index ϕ

https://doi.org/10.5194/jecats-2026-12
Preprint. Discussion started: 28 July 2026

5 Solution Methodology for Single-Plume Evolution

Although the governing equations (Eqs. 3) are inherently three-dimensional, requiring a fully resolved 3D mesh and often forcing a trade-off between resolution and domain size, the system admits a separable structure under physically justified assumptions. Exploiting this separability permits high-resolution solutions over extended domains without resorting to coarse-grained approximations and high computational times.

We initialize the contrail by releasing ice particles into a three-dimensional region immediately following the earlier stages that the contrail has been through (roughly, after a few minutes of contrails birth), prescribing initial fields as:

$$c_N(\mathbf{x},0) = c_{N,0}, \quad m(\mathbf{x},0) = m_0, \quad \phi(\mathbf{x},0) = \phi_0. \tag{10}$$

The volumetric growth rate $f_{\mathcal{V}}$ depends on ambient temperature $T(x,y,z,t)$, but observational datasets typically have horizontal resolution of order kilometers and exhibit weak horizontal gradients. Accordingly we assume $T = T(z,t)$, and, $s_i = s_i(z,t)$, yielding $f_{\mathcal{V}} = f_{\mathcal{V}}(z,t)$ and $m = m(z,t)$.

Therefore, we adopt the following separable ansatz:

$$c_N(x,y,z,t) \;=\; F(x,y,t)\, g(z,t), \tag{11}$$

with a closure for the turbulent diffusivities $\widetilde{\mathcal{D}}_{xx}$, $\widetilde{\mathcal{D}}_{yy}$, and $\widetilde{\mathcal{D}}_{zz}$.

Moreover, we note that the relative humidity in the expanding contrail core may remain close to ice saturation because entrainment of fresh, unsaturated air typically occurs on a longer timescale (minutes to hours) than crystal growth (seconds to minutes). To represent this effect in our model we employ an auxiliary equation which is considered as the first-order approximation for the differential equation associated with the ice-supersaturation balance.

Enforcing vanishing fluxes at $x,y \to \pm\infty$ and $z \to \pm\infty$ together with the normalization $\int_{-\infty}^{+\infty} g(z,t)\,\mathrm{d}z = 1$, and the system decouples into:

https://doi.org/10.5194/jecats-2026-12
Preprint. Discussion started: 28 July 2026

$$\left\{ \frac{\partial F}{\partial t} + w_x(x,y,t)\frac{\partial F}{\partial x} + w_y(x,y,t)\frac{\partial F}{\partial y} = \widetilde{\mathcal{D}}_{xx}\frac{\partial^2 F}{\partial x^2} + \widetilde{\mathcal{D}}_{yy}\frac{\partial^2 F}{\partial y^2} \right\} \rightarrow \textbf{horizontal ADE (Eulerian tracker)}.$$

$$\left.\begin{cases} \dfrac{\partial g}{\partial t} + v_s(z,t)\,\dfrac{\partial g}{\partial z} = \widetilde{\mathcal{D}}_{zz}\dfrac{\partial^2 g}{\partial z^2} - g\dfrac{\partial v_s}{\partial z}, \\ \dfrac{\partial m}{\partial t} + v_s(z,t)\,\dfrac{\partial m}{\partial z} = \widetilde{\mathcal{D}}_{zz}\dfrac{\partial^2 m}{\partial z^2} + \dfrac{2\,\widetilde{\mathcal{D}}_{zz}(g)}{g}\,\dfrac{\partial m}{\partial z}\,\dfrac{\partial g}{\partial z} + \rho_{\mathrm{dep}}\,f_{\mathcal{V}}(z,t), \\ \dfrac{\partial \phi}{\partial t} + v_s(z,t)\,\dfrac{\partial \phi}{\partial z} = \dfrac{\Gamma^*\big(T(z,t),s_i(z,t)\big) - 1}{\Gamma^*\big(T(z,t),s_i(z,t)\big) + 2}\,\dfrac{\phi}{\mathcal{V}}\,f_{\mathcal{V}}(z,t) - \phi\dfrac{\partial v_s}{\partial z}, \\ \dfrac{\partial s_i}{\partial t} = -\dfrac{1}{q_s}\dfrac{S_{\mathrm{dep}}}{\rho_{\mathrm{air}}} - \dfrac{1+s_i}{q_s}\dfrac{\partial q_s}{\partial t} + \dfrac{s_{\mathrm{env}} - s_i}{\tau_{\mathrm{entrain}}}, \\ |v_s(z,t)| = v_{\mathbf{ter}}\,\dfrac{q_0(z,t)}{q_0(z,t)+q_1(z,t)}, \\ q_0(z,t) = \mathrm{erfc}\big(\dfrac{\Delta_0 - v_{\mathbf{ter}}t}{2\sqrt{\nu_{\mathbf{t,ef}}t}}\big)\exp\Big(\dfrac{v_{\mathbf{ter}}^2 t}{4\nu_{\mathbf{t,ef}}} - \dfrac{v_{\mathbf{ter}}\Delta_0}{2\nu_{\mathbf{t,ef}}}\Big), \\ q_1(z,t) = \mathrm{erfc}\big(-\dfrac{\Delta_0}{2\sqrt{\nu_{\mathbf{t,ef}}t}}\big), \quad \Delta_0 = z - z_{\mathbf{relax}}, \\ \mathrm{d}X = -\dfrac{X-\mu}{\tau}\,\mathrm{d}t + \sigma_X\,\mathrm{d}W_t, \quad X \in \{\tilde{\mathcal{D}}_{xx}, \tilde{\mathcal{D}}_{yy}, \tilde{\mathcal{D}}_{zz}, v_s\}, \\ \mathcal{V}(z,t) = \dfrac{m(z,t)}{\rho_{dep}}. \end{cases}\right\} \rightarrow \textbf{plume evolution in } z\textbf{-}t \textbf{ space}. \qquad (12)$$

where $S_{\mathrm{dep}} = c_N\rho_{\mathrm{dep}}\,f_{\mathcal{V}}$ represents the supersaturation depletion/recovery rate by ice growth/sublimation. Moreover, $s_{\mathrm{i,env}}$ denotes the supersaturation of the environment and τ_{entrain} is the effective recovery/relaxation timescale, and q_s is water-vapor mixing ratio (see Appendix G for the derivation details). Reviewing the above equations, one notes that the horizontal ADE is still weakly coupled to the plume evolution in z-t space through c_N and τ_{entrain}, which are geometrical variables. However, if the cylindrical plume hypothesis is adopted, as in Schumann (2012), these geometrical variables can be estimated for single-plume cross-sectional diffusion using standard kernels, thereby making the horizontal tracking completely decoupled from the plume evolution in z-t space.

Remark 1: In this research, we solve only the plume evolution in z-t space by decoupling it from the horizontal ADE, and the PDEs are solved using an implicit tridiagonal matrix algorithm (TDMA).

Remark 2: When the horizontal ADE is decoupled from the plume evolution in z-t space, it can be replaced by Lagrangian plume-center tracking in single-flight assessments.

Remark 3: When moving from single-plume to single-flight assessments, the horizontal ADE can be advantageous over Lagrangian plume-center tracking, as it provides more accurate advection–diffusion coupling in the horizontal plane and can capture interactions between coexisting plumes. Moreover, c_N and τ_{entrain} can revert to their original coupled mode, thereby improving the accuracy of the plume evolution in z-t space.

https://doi.org/10.5194/jecats-2026-12
Preprint. Discussion started: 28 July 2026

Notably, the initial time $(t=0)$ corresponds to the onset of the long-term diffusion regime. Consequently, the solver requires estimates of $g(z,t=0)$, $m(z,t=0)$, $\phi(z,t=0)$, as well as $\sigma_y(t=0)$. We assume $\phi(z,t=0)=1$ (i.e., spherical assumption), and $g(z,t=0)$ is considered Gaussian. With these, the initial conditions reduce to:

1) the mean particle radius $a(t=0)$ which is used to compute $m(t=0)=(4/3)\pi(a(t=0))^3\rho_{ice}$,

2) vertical standard deviation $\sigma_z(t=0)$ which is used to compute $g(z,t=0)=\frac{1}{(\sigma_z(t=0))\sqrt{2\pi}}\exp\left(-\frac{z^2}{2(\sigma_z(t=0))^2}\right)$,

3) per meter soot emission after passing the vortex regime n_{line}, and cross-sectional standard deviation $\sigma_y(t=0)$ used in approximating $c_N \approx \frac{n_{line}}{\sqrt{2\pi}\sigma_y(t)}g(z,t)$, with $\sigma_y(t)=\sqrt{(\sigma_y(t=0))^2+2\widetilde{\mathcal{D}}_{yy}t}$.

In general, these quantities can be obtained from existing early-stage parameterizations, such as CoCiP, Schumann (2012). Nonetheless, in this research, we are more interested in varying some of the initial conditions within a physically realistic range and exploring the spectrum of different solutions that the above PDE system can yield.

6 Results and Discussions

We first assess convergence of the plume evolution and establish a corresponding resolution threshold. As a metric sensitive to vertical discretization, we consider the time-averaged center-of-mass height, defined as $\overline{z}_{\mathrm{cm}}=\frac{1}{T}\int_0^T z_{\mathrm{cm}}(t)\,\mathrm{d}t$, where $T=10$ h. In discrete form, this is approximated as $\overline{z}_{\mathrm{cm}}\approx\frac{1}{N}\sum_{n=1}^{N}z_{\mathrm{cm}}(t_n)$.

A high-resolution simulation with $\Delta t_{\mathrm{ref}}=1$ s and $\Delta z_{\mathrm{ref}}=0.5$ m is taken as the reference solution, denoted $\overline{z}_{\mathrm{cm}}^{\mathrm{ref}}$. The relative error for a given discretization $(\Delta z,\Delta t)$ is defined as $\varepsilon(\Delta z,\Delta t)=\frac{\left|\overline{z}_{\mathrm{cm}}(\Delta z,\Delta t)-\overline{z}_{\mathrm{cm}}^{\mathrm{ref}}\right|}{\left|\overline{z}_{\mathrm{cm}}^{\mathrm{ref}}\right|}\times 100\%$.

We note that the vertical solver exhibits weak sensitivity to the time step for $\Delta t \lesssim 50$ s. Accordingly, convergence test is performed with $\Delta t=10$ s while varying Δz. We observe that reducing the vertical grid spacing to approximately $\Delta z\approx 3$ m yields convergence within 1% relative error (see Fig. 3a). Therefore, for the simulations presented in this section, the z-domain from $+1000$ m to -2500 m is discretized using 2000 grid cells, corresponding to a uniform grid spacing of $\Delta z=1.75$ m.

Figure 3b shows the computational time of the PDE solver in $z-t$ space over a 10-hour simulation as a function of the solver time step, for several vertical resolutions. When the present Eulerian framework is deployed in large-scale analyses involving many plumes (e.g., using the horizontal ADE or the Lagrangian plume tracker– see Sec. 5), the vertical PDE solver remains the dominant contributor to overall computational cost. Although this study does not target large-scale applications, the timings in Fig. 3b indicate that the model is promising for such scenarios. As can be seen, for moderate vertical resolution and solver time step, the computational time of the vertical solver can fall below one second.

https://doi.org/10.5194/jecats-2026-12
Preprint. Discussion started: 28 July 2026

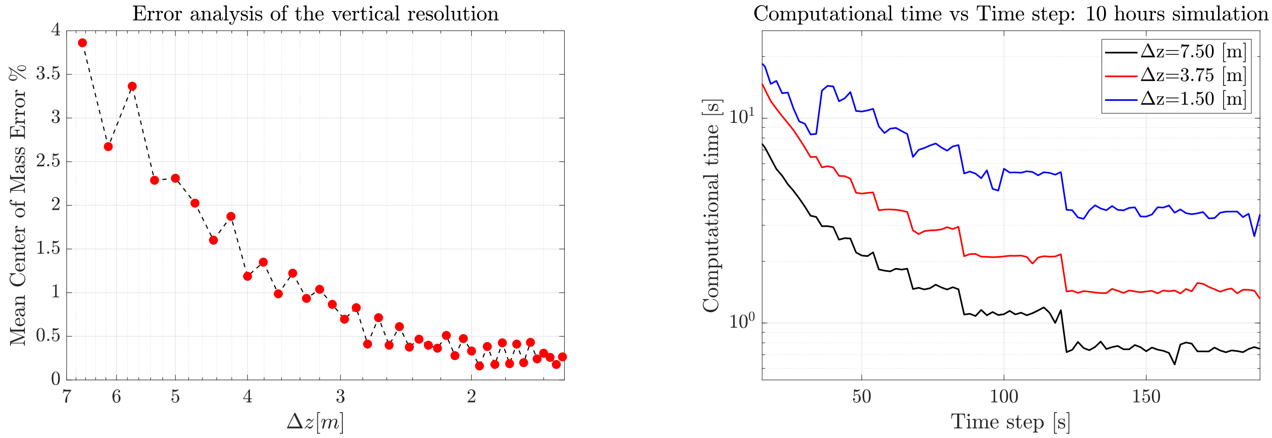

(a) Vertical-resolution convergence of the 10-hour mean center-of-mass position

(b) Computational time of the vertical solver for a 10-hour simulation as a function of time step

Figure 3. Vertical-resolution convergence and computational cost analysis.

To demonstrate the performance of the plume solver, we consider three comparative scenarios: (i) varying the line ice-particle number emission index, n_{line} (particles m^{-1}); (ii) varying the background supersaturation, s_{env}; and (iii) varying the initial vertical plume standard deviation, $\sigma_z(t=0)$. In all simulations, the initial mean ice-particle radius is prescribed as $a(z,t=0) = 1\ \mu$m, the initial habit parameter is set to $\phi(z,t=0) = 1$, corresponding to spherical ice crystals, and the initial horizontal plume standard deviation is fixed at $\sigma_y(t=0) = 10$ m. Moreover, the vertical and horizontal diffusion coefficients are set as $D_{zz} = 0.1m^2/s$, and $D_{yy} = 15m^2/s$ respectively, in our simulations. For each scenario, the solution is presented as contour plots in the z–t plane at different times.

Case 1: Varying Per Meter Initial Number Concentration n_{line}. In this case, we consider a supersaturated layer extending from $z = -200$ to $z = 200$, where $z = 0$ denotes the reference altitude at which the plume is initially released. Specifically, $s_{\text{env}}(-200 \leq z \leq 200, \forall t) = 0.1$, while $s_{\text{env}} = -0.15$ elsewhere. The temperature at the reference altitude is fixed at 222 K, and its vertical profile follows the standard atmospheric lapse rate. The corresponding contour plots are presented in Fig. 4, and 5.

Although the experiment is based on an idealized configuration with a fixed reference temperature and a temporally invariant supersaturation field, comparison of the cases with $n_{\text{line}} = 10^{10}$ and $n_{\text{line}} = 10^{11}$ shows that the latter produces a longer-lived contrail despite exhibiting a lower optical depth. Physically, a larger n_{line} accelerates the depletion of the available supersaturation, thereby limiting the growth of individual ice crystals. Consequently, larger values of n_{line} produce a greater number of smaller ice crystals that remain suspended for longer owing to their lower settling velocities, particularly when they retain plate-like morphologies. Conversely, crystals with more columnar shapes may leave the supersaturated layer more rapidly despite having similar masses, owing to their higher settling velocities. Thus, the present model does not assign a unique settling velocity to crystals of equal mass; instead, crystal

https://doi.org/10.5194/jecats-2026-12
Preprint. Discussion started: 28 July 2026

geometry plays a fundamental role in determining the settling behavior. In addition, crystal habit also influences the growth and sublimation rates by modifying parameters such as ice crystal capacitance.

Finally, because the governing PDE system is strongly nonlinear and tightly coupled, variations in the environmental conditions as well as the initial and boundary conditions produce substantially different spatial and temporal plume distributions. In the present simulations, the plume center naturally remains near the upper portion of the plume owing to the fall streak of heavier, predominantly columnar crystals, which exhibit higher settling velocities, particularly at low Reynolds numbers. As these crystals rapidly leave the supersaturated region and sublimate, the upper portion of the plume persists for a longer period.

Case 2: Varying Ice Supersaturation s_{env}. In this case, we consider two supersaturated layers extending from $z = -200$ to $z = 200$, where $z = 0$ denotes the reference altitude at which the plume is initially released. Specifically, $s_{\text{env}}(-200 \leq z \leq 200, \forall t) = 0.05\textbf{or}0.25$, while $s_{\text{env}} = -0.15$ elsewhere. The temperature at the reference altitude is fixed at 230 K, and its vertical profile follows the standard atmospheric lapse rate. Moreover, $n_{\text{line}} = 3 \times 10^{10}$, and $\sigma_z(t = 0) = 20$. The corresponding contour plots are presented in Fig. 6, and 7.

From these figures, we observe that a higher environmental supersaturation generally leads to faster ice crystal growth and higher local settling velocities. However, these larger crystals leave the supersaturated layer more quickly, resulting in a shorter contrail lifetime in this example. Nevertheless, the ice mass concentration for the case of $s_{env} = 0.25$ reaches up to approximately ten times that of the $s_{env} = 0.05$ case during the first hour of the long-term diffusion regime.

Case 3: Varying Initial Vertical Plume Standard Deviation $\sigma_z(t = 0)$. In this case, we consider the supersaturated layer extending from $z = -200$ to $z = 200$, where $z = 0$ denotes the reference altitude at which the plume is initially released. Specifically, $s_{\text{env}}(-200 \leq z \leq 200, \forall t) = 0.2$, while $s_{\text{env}} = -0.15$ elsewhere. The temperature at the reference altitude is fixed at 222 K, and its vertical profile follows the standard atmospheric lapse rate. Moreover, $n_{\text{line}} = 3 \times 10^{10}$, while the initial vertical plume standard deviation varies. Specifically, we consider two distinct cases of $\sigma_z(t = 0) = 5$ and $\sigma_z(t = 0) = 60$. The corresponding contour plots are presented in Fig. 8, and 9. From these figures, we observe that the nonlinear behavior of the plume is more pronounced for the case of $\sigma_z(t = 0) = 60$. This is primarily because the initially wider plume is more exposed to the background conditions, causing different plume slices to undergo distinct growth, sublimation, and settling trajectories. In this particular example, the larger initial value of $\sigma_z(t = 0)$ results in a more pronounced fall streak of the ice crystals and a slight displacement of the peak ice water concentration.

On computing the contrail optical depth as $\tau(t) = \int \beta_{\text{ext}}(z)\,\mathrm{d}z = \int Q_{\text{ext}}\,\overline{A}_{\text{proj}}(z)\,c_N(z)\,\mathrm{d}z$, where β_{ext} is the volume extinction coefficient (m^{-1}), Q_{ext} is the extinction efficiency (taken as 2 in the geometric optics limit), and $\overline{A}_{\text{proj}}$ is the orientation-averaged projected area of an ice particle (m^2), we define the optical-depth ratio as

$$\textbf{Ratio} = \frac{\int_0^{t^*} \tau_h(t)\,\mathrm{d}t}{\int_0^{t^*} \tau_s(t)\,\mathrm{d}t},$$

https://doi.org/10.5194/jecats-2026-12
Preprint. Discussion started: 28 July 2026

where t^* denotes the time at which the contrail optical depth first falls below 0.001. Here, $\tau_s(t)$ is the optical depth obtained with the habit evolution equation disabled, corresponding to spherical particles ($\phi = 1$) throughout the simulation, whereas $\tau_h(t)$ is obtained from the fully coupled solution of the z-t PDE system with dynamic habit evolution.

The analysis is restricted to a representative test case with $n_{\text{line}} = 3 \times 10^{10}$ m^{-1}, $\sigma_z(t=0) = 20$ m, $\sigma_y(t=0) = 10$ m, and an initial particle size of $a(z,t=0) = 1$ μm. Three different constant values of s_{env} are prescribed within the layer extending from -200 m to $+200$ m, while $s_{\text{env}} = -0.05$ is imposed outside this region. The resulting values of **Ratio** are shown in Fig. 10.

Figure 10 indicates that dynamic habit evolution can modify the time-integrated contrail optical depth. However, these results should be regarded as preliminary. A more comprehensive assessment requires the inclusion of additional physical processes, such as ventilation effects and morphological evolution (e.g., hollowing and branching), together with further calibration of the habit parameterization, particularly under conditions of low ice supersaturation (see Appendix E). Furthermore, the analysis is based on a synthetic initial condition and therefore does not necessarily represent the full range of possible contrail behavior.

Despite these limitations, the results suggest that neglecting the dynamic coupling between ice crystal habit evolution and the growth, sublimation, and settling processes may lead to appreciable errors in the prediction of key contrail properties, including the ice water content, optical depth, and consequently the radiative forcing. These findings emphasize the importance of incorporating a physically consistent, time-dependent habit parameterization into contrail models.

https://doi.org/10.5194/jecats-2026-12
Preprint. Discussion started: 28 July 2026

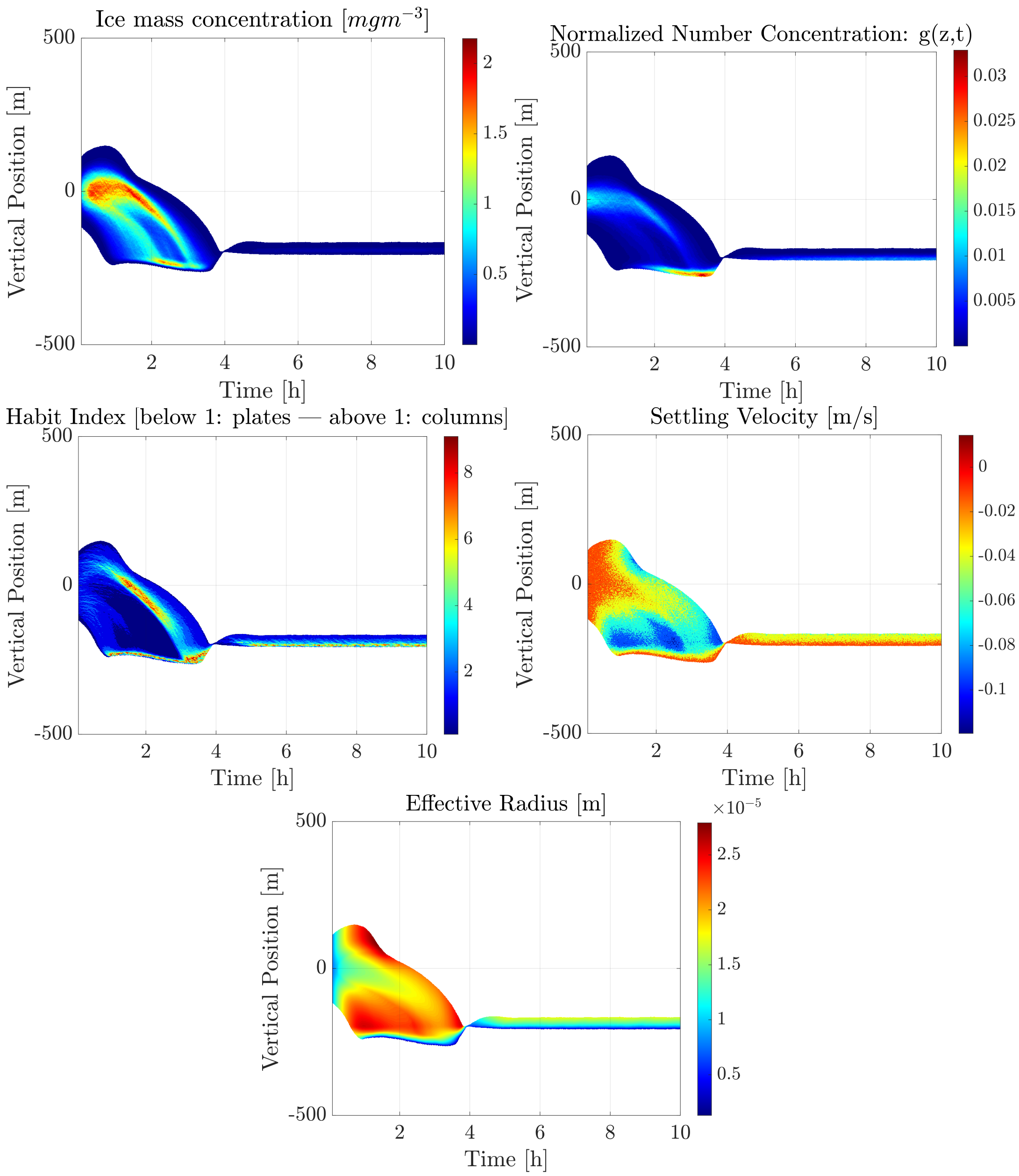

Figure 4. Case 1: $n_{line} = 10^{10}$

https://doi.org/10.5194/jecats-2026-12
Preprint. Discussion started: 28 July 2026

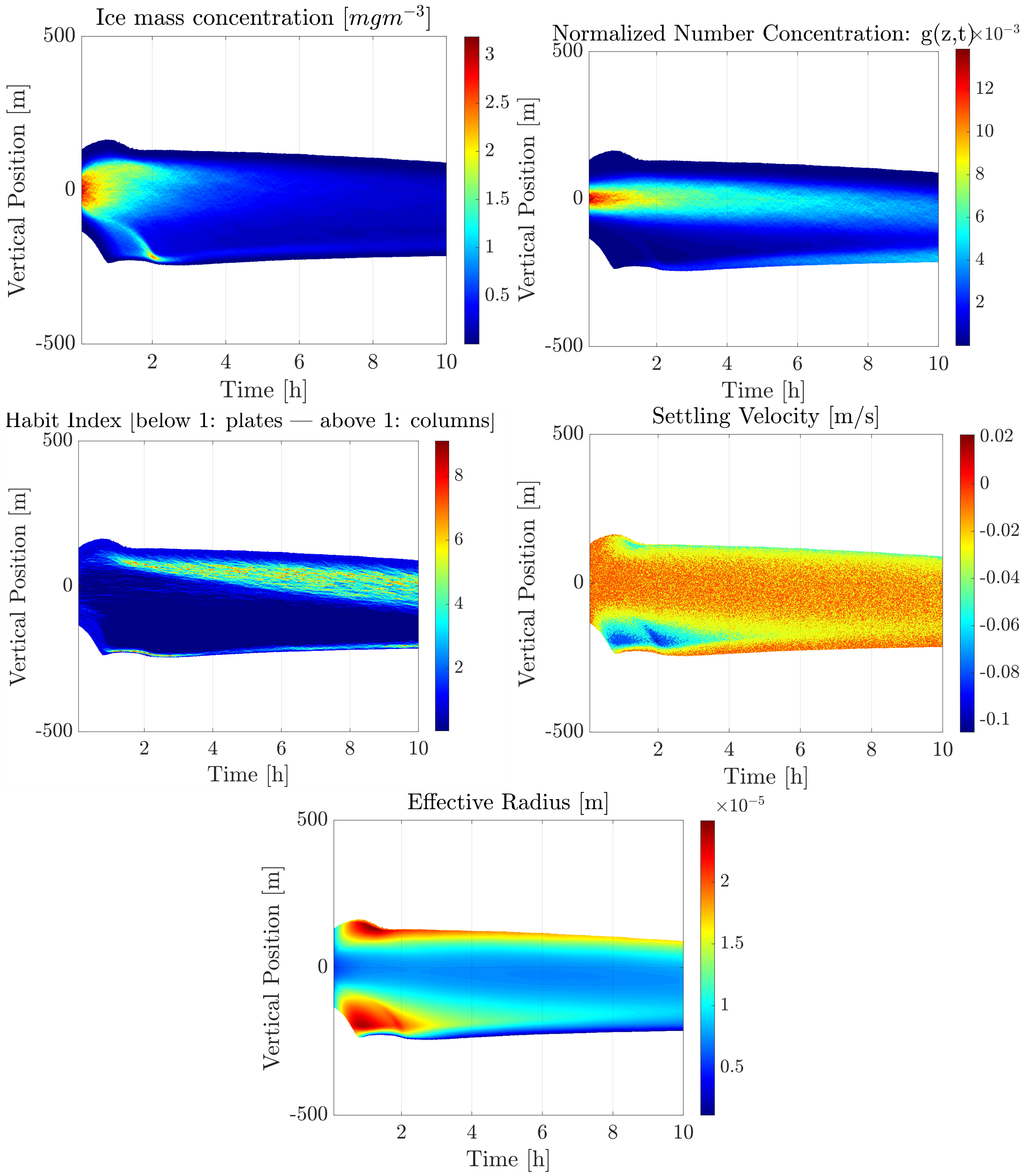

Figure 5. Case 1: $n_{line} = 10^{11}$

https://doi.org/10.5194/jecats-2026-12
Preprint. Discussion started: 28 July 2026

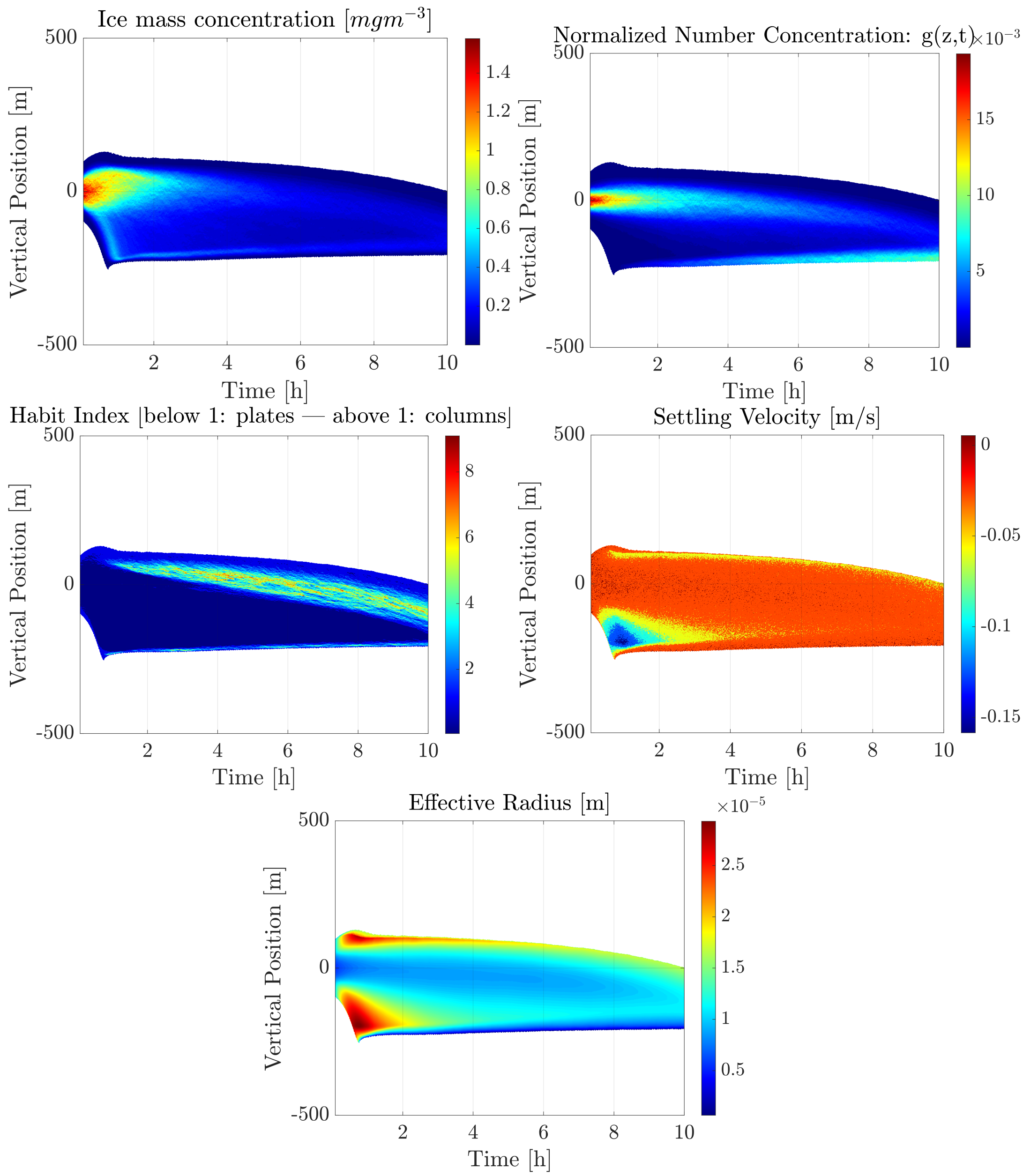

Figure 6. Case 2: $s_{env} = 0.05$

https://doi.org/10.5194/jecats-2026-12
Preprint. Discussion started: 28 July 2026

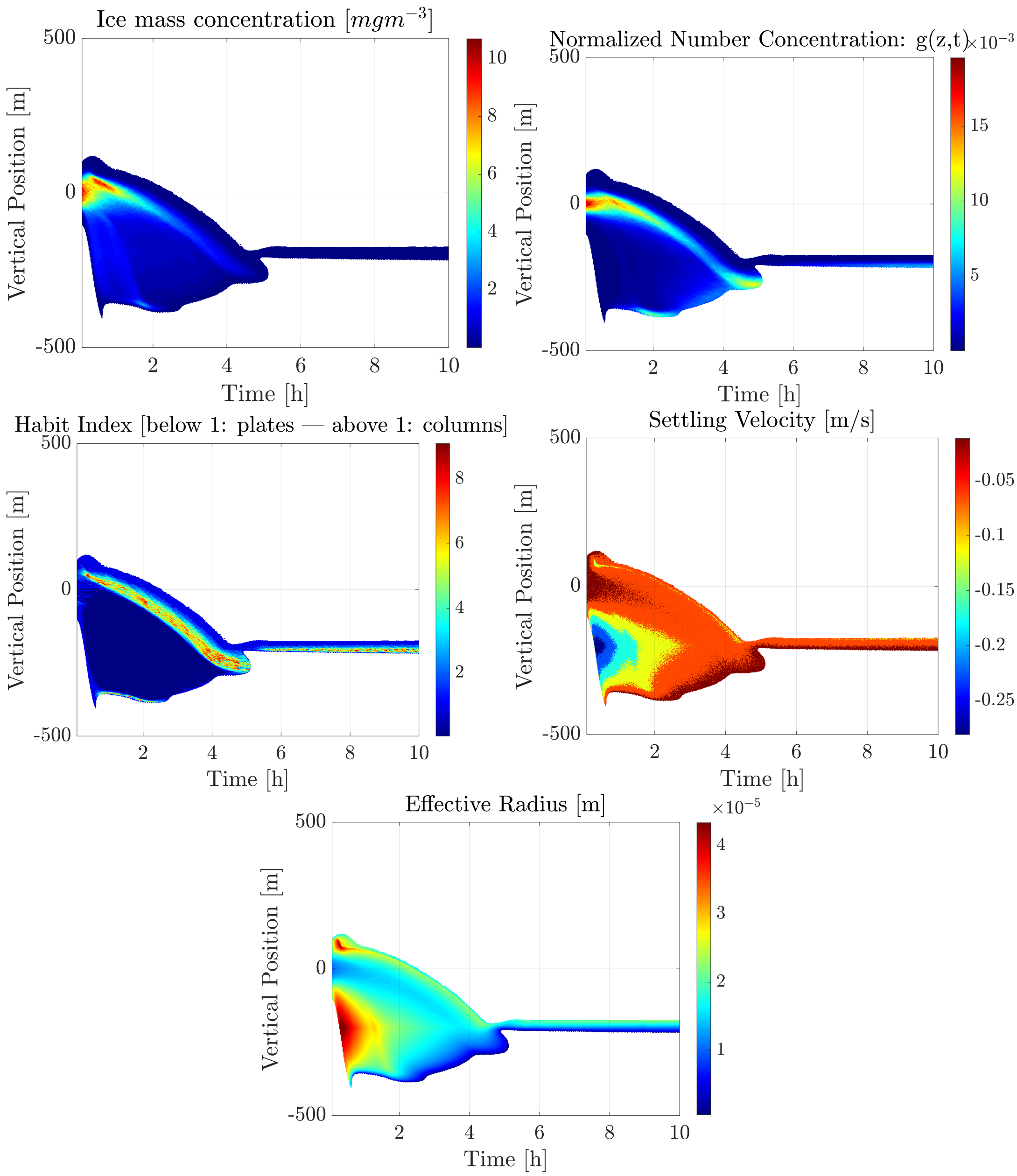

Figure 7. Case 2: $s_{env} = 0.25$

https://doi.org/10.5194/jecats-2026-12
Preprint. Discussion started: 28 July 2026

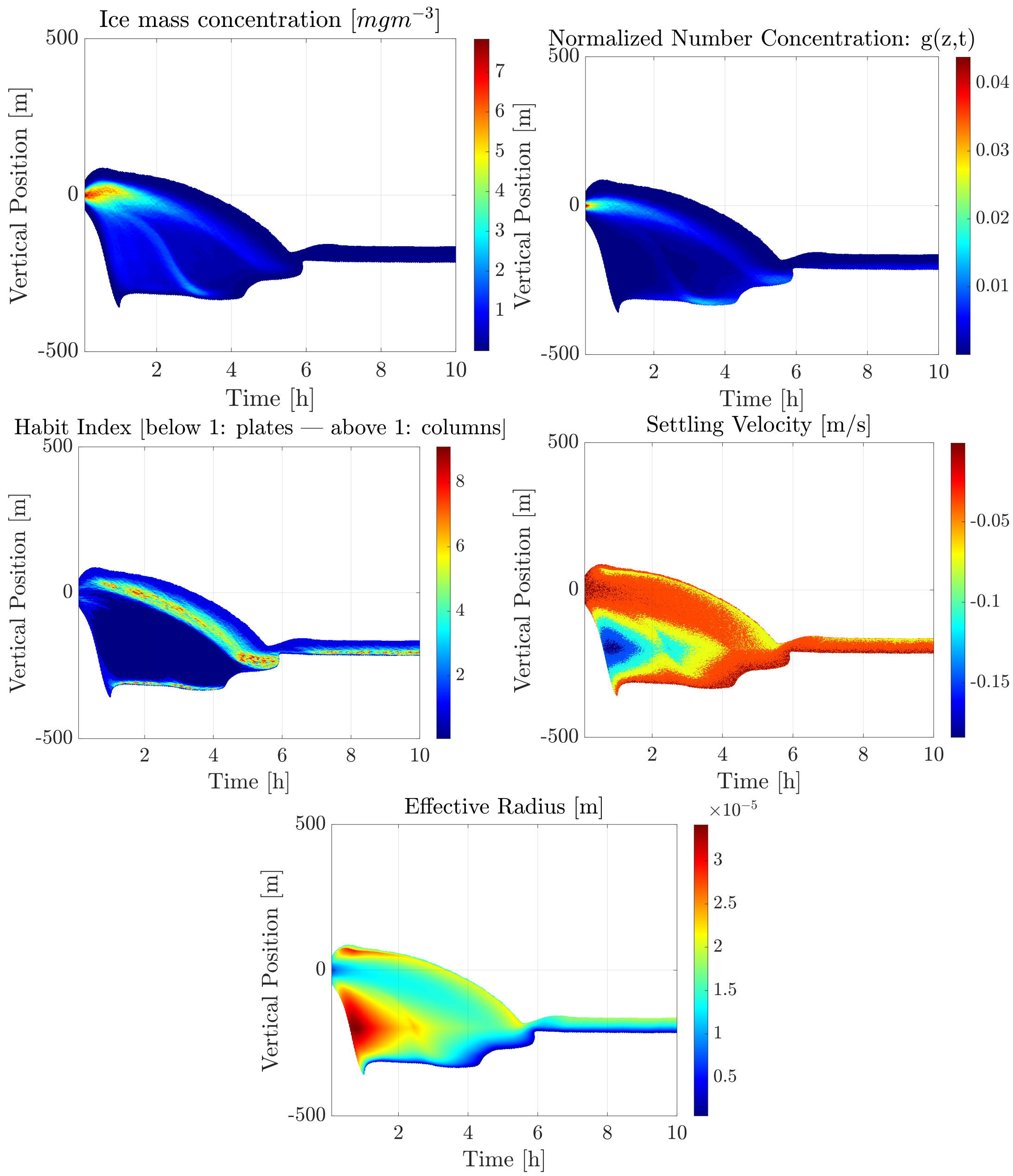

Figure 8. Case 3: $\sigma_z(t=0)=5$

https://doi.org/10.5194/jecats-2026-12
Preprint. Discussion started: 28 July 2026

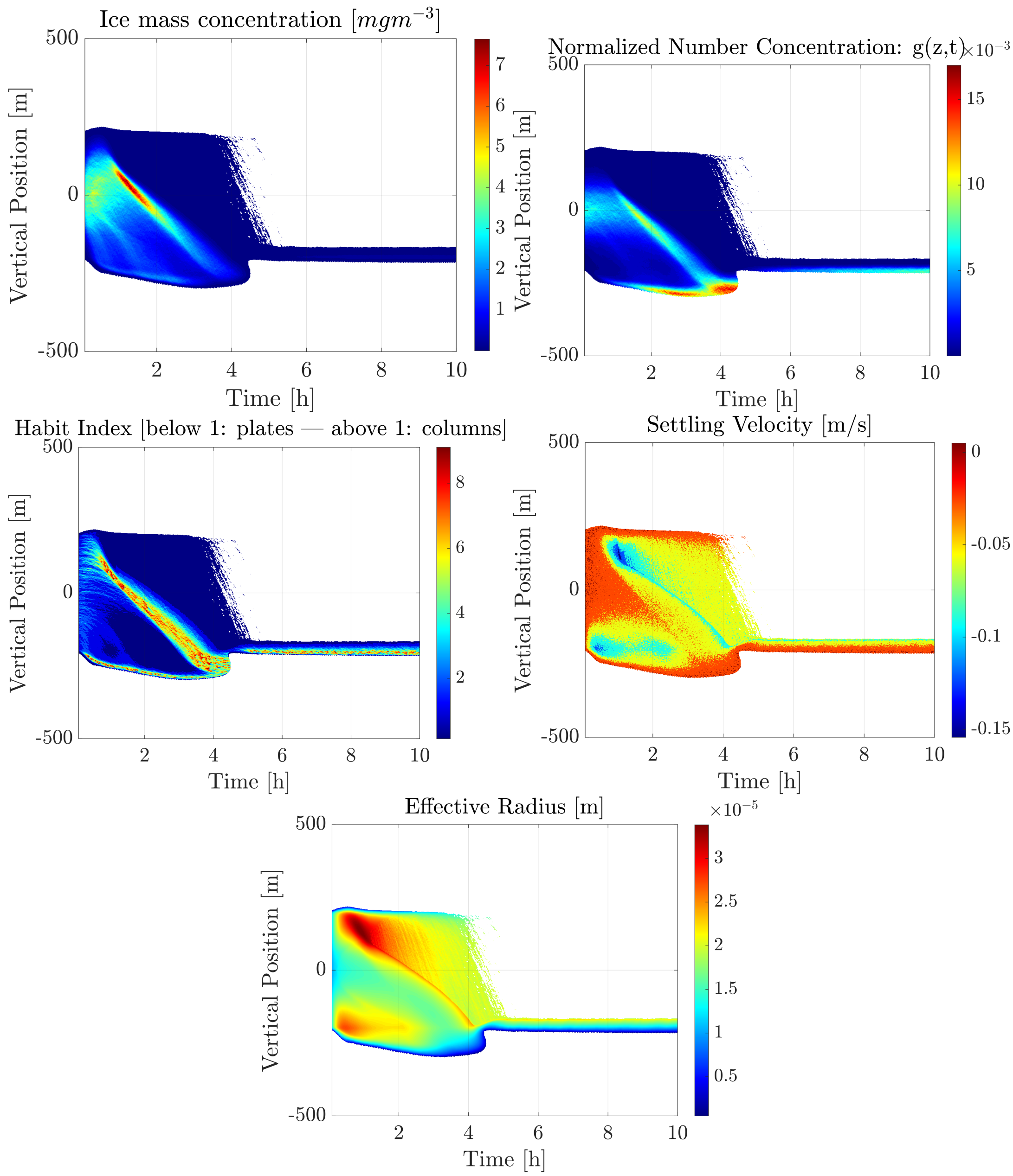

Figure 9. Case 3: $\sigma_z(t=0) = 60$

https://doi.org/10.5194/jecats-2026-12
Preprint. Discussion started: 28 July 2026

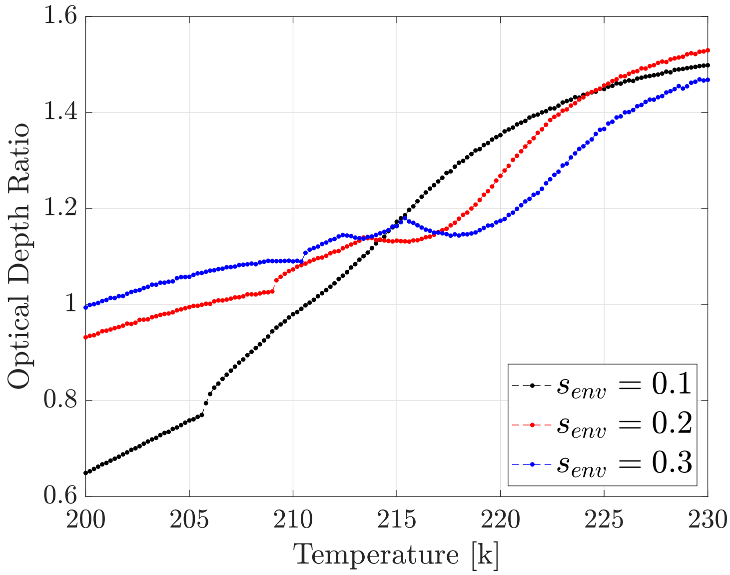

Figure 10. Ratio of the time-integrated contrail optical depth predicted by the habit-evolution model to that predicted by the spherical-particle model.

6.1 Comparison with CoCiP and Further Discussions

In this section, we present a preliminary visual comparison of the present model with CoCiP. To enable an approximate comparison, we first note that CoCiP represents contrail segments as Lagrangian Gaussian plumes in the plane perpendicular to the flight direction and evolves bulk per-length scalar quantities via ODEs. Specifically, CoCiP prognoses the ice water mass per unit length, the total ice-particle number per unit length, and the plume covariance matrix , from which the effective cross-sectional widths (e.g., lateral width and vertical depth, or equivalently σ_y and σ_z) are obtained. The corresponding centerline volume concentrations are diagnosed from these per-length quantities using the Gaussian cross-sectional area. As a result, CoCiP reports per-meter bulk quantities and does not explicitly resolve the three-dimensional concentration field; instead, the plume geometry emerges diagnostically from the evolved bulk variables Schumann (2012) [5].

For comparison purposes, we design a synthetic CoCiP setup and use the same early-stage parametrization of the plume in MultiCon Schumann (2012). The CoCiP specifications used in this comparison are listed in Table H1. Finally, because the separation ansatz employed in MultiCon prevents direct resolution of wind-shear effects, we account for wind shear by applying the method of characteristics (see Appendix H).

[5] Notably, CoCiP does not explicitly resolve along-track diffusion. Instead, contrail segments are represented as extruded Gaussian cross-sections, whose elongation in the flight (x) direction reflects the chosen integration length of each segment. In contrast, the MultiCon model can directly resolve the three-dimensional plume geometry through the vertical PDEs and the horizontal ADE, while explicitly accounting for along-track diffusion. This induces modest variations in the ice number concentration along the x-direction. However, as discussed earlier, the advantages of the horizontal ADE are most pronounced in single-flight assessments, where it enables an explicit analysis of plume interactions under continuous emissions. Therefore, in the present study, we rely on the solution of the vertical PDEs in a decoupled mode (see Sec. 5).

https://doi.org/10.5194/jecats-2026-12
Preprint. Discussion started: 28 July 2026

In general, the topological property of the plume in CoCiP remains a Gaussian kernel throughout the entire plume lifetime. However, by directly resolving the plume geometry, the MultiCon model can predict a variety of plume shapes depending on environmental and initial conditions. The general trend observed in MultiCon can be summarized as follows: ice crystals may transition into plates and columns depending on the local temperature, supersaturation, and particle's mass/shape history. Column-like crystals leave the ISSR thickness more rapidly, and the plume core tends to relax toward plate-like crystals with slower settling velocities. This behavior can sometimes lead to a slight oscillation in the settling of the center of mass.

To illustrate, the transformation process between column- and plate-like crystals is strongly nonlinear and depends on multiple factors, among which we observe a stronger dependence on the local ice supersaturation. Specifically, as column-like crystals leave the ISSR, they deplete the local water vapor at a higher rate compared to plate-like crystals. During this phase, the center of mass remains almost monotonically decreasing. However, as column-like crystals exit the ISSR, plate-like crystals begin to dominate the plume core by uptaking the remaining water vapor while descending slowly. This later dominant role of plate-like crystals can shift the center of mass upward, and depending on the time-scale of the involved nonlinear processes, this may also lead to a weakly damped oscillation, with maximum amplitudes reaching tens of meters in some cases.

A visual comparison between the IWC and number concentration predicted by CoCiP after two hours of simulation and those predicted by the present model is shown in Fig. 11. The slight difference in the number concentration peak may be related to the different diffusion schemes, which further affect the IWC computation. However, when visually comparing the plume core while considering both number and mass concentration, one may observe that, under the specified environmental setup, the averaged individual ice crystal mass predicted by MultiCon is nearly an order of magnitude higher than that predicted by CoCiP. Nevertheless, more definitive conclusions require a separate, dedicated study, also accounting for potential microphysical refinements and parameter-range tuning of MultiCon. In addition, Fig. 12 shows a comparison of the plume center-of-mass settling between the two models.

It should be emphasized that a more rigorous comparison will be presented in a separate paper, in which an enhanced version of MultiCon, incorporating additional physical processes such as ventilation effects, detailed ice crystal habit morphologies, and polydispersity, will be compared with CoCiP in a more comprehensive and systematic manner.

https://doi.org/10.5194/jecats-2026-12
Preprint. Discussion started: 28 July 2026

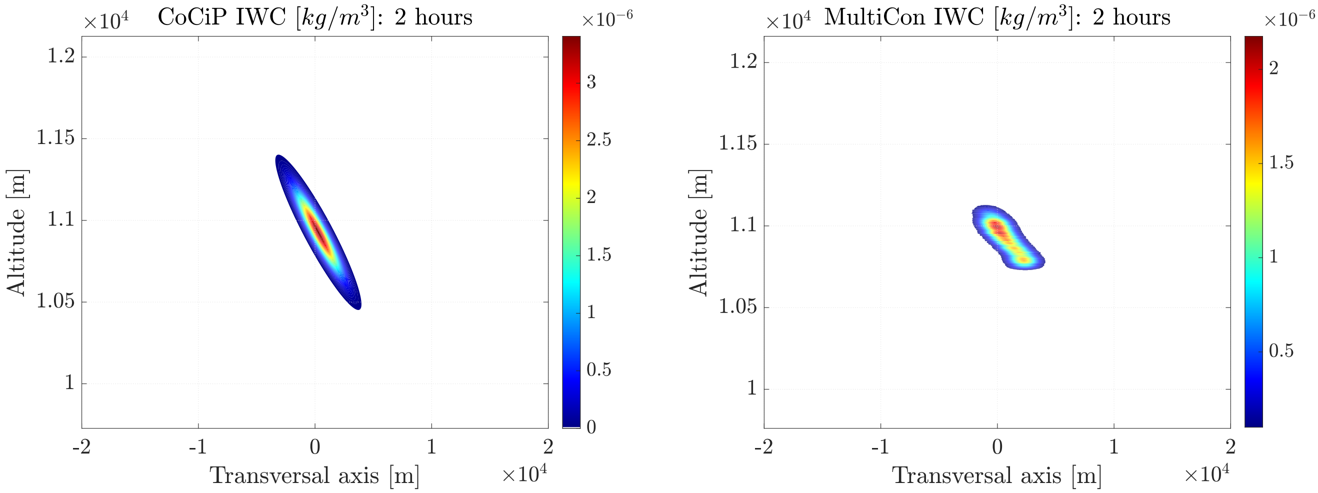

(a) CoCiP IWC: 2 hours

(b) MultiCon IWC: 2 hours

Figure 11. MultiCon compared with CoCiP

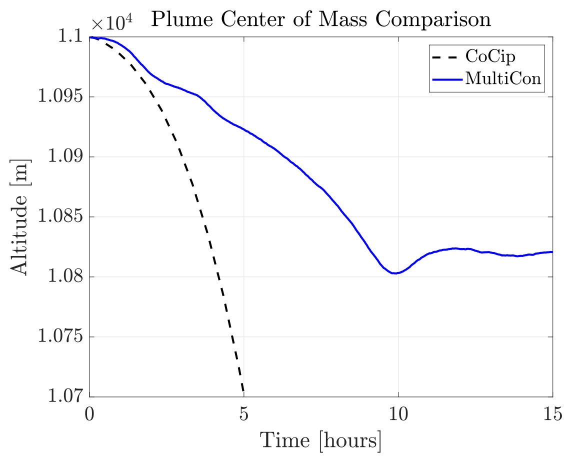

Figure 12. Center of mass comparison between CoCiP and MultiCon

7 Conclusion

We presented an Eulerian, multi-physics framework for long-term contrail evolution that retains two moments of the population-balance equation (PBE), thereby ensuring conservation of particle number and mass. The model incorporates a settling-velocity formulas accounting for the bulk settling of ice crystals in turbulent flows, together with a habit-tracking field equation dynamically coupled to the microphysical growth and gravitational settling equations in a spatio-temporally resolved PDE framework. Under mild regularity assumptions the governing system

https://doi.org/10.5194/jecats-2026-12
Preprint. Discussion started: 28 July 2026

admits a separable structure, which makes the model well suited for large-scale simulations by striking a favorable balance between accuracy and computational cost.

Notably, the vertical solver can be extended to treat particle mass explicitly and represent polydispersity; with low-parameter closures, the additional computational cost remains modest. Moreover, microphysical fidelity may be increased by augmenting the growth and habit-dynamics terms to include habit-specific ventilation corrections, and morphological evolution (e.g., hollowing or branching) which directly modifies deposition density.

We suggest prioritizing the calibration of model parameters that carry the largest uncertainties by tuning against available contrail observations (for example, in-plume measurements or radiative-forcing diagnostics). Both theoretical analysis and numerical experiments indicate that the newly introduced ingredients, particularly bulk settling and explicit habit dynamics, may considerably influence integral plume properties. In particular (supported by the extensive set of simulations conducted throughout this study), the habit-resolving model exhibits notable deviations in optical depth relative to a spherical-particle baseline.

Therefore, the proposed framework provides a computationally tractable, physically consistent basis for exploring various micro/macro-physics effects and for systematic model–data integration in future studies.

Finally, we emphasize that the single-plume solver presented in this study, while still amenable to further improvements through the inclusion of the aforementioned physical processes, is readily scalable to global contrail assessments owing to its high computational efficiency (roughly, less than one second per plume). Two principal approaches for extending the single-plume framework to global-scale simulations are also discussed in Sec. 5 of this paper.

Data Availability Statement

The main modeling code and separate scripts for generating the figures presented in this paper are publicly available at the following repository, enabling reproduction of the results reported in this study: link

Conflict of Interest

The authors declare no conflict of interest of any type within the present submission.

Acknowledgment

The authors acknowledge financial support from Project CLIMATION (PID2024-158160OB-C31), funded by the Spanish Ministry of Science and Innovation. The authors greatly appreciate the anonymous reviewers for their valuable comments and suggestions, which helped improve the manuscript. The authors express their sincere gratitude to Dr. Caleb Akhtar Martínez (University of Cambridge) for his generous and insightful guidance on APCEMM and CoCiP, as well as for valuable scientific discussions. The authors also gratefully acknowledge Mr. Oumarou Moussa Bola and Prof. Abolfazl Simorgh (Universidad Carlos III de Madrid) for their kind support with the PyContrails implementation and analysis of CoCiP outputs.

https://doi.org/10.5194/jecats-2026-12
Preprint. Discussion started: 28 July 2026

References

Engberg, Z., Teoh, R., Abbott, T., Dean, T., Stettler, M. E. J., and Shapiro, M. L.: Forecasting contrail climate forcing for flight planning and air traffic management applications: the CocipGrid model in pycontrails 0.51.0, Geoscientific Model Development, 18, 253–286, https://doi.org/10.5194/gmd-18-253-2025, 2025.

Paoli, R. and Shariff, K.: Contrail modeling and simulation, Annual Review of Fluid Mechanics, 48, 393–427, https://doi.org/10.1146/annurev-fluid-010814-013619, 2016.

Akhtar Martinez, C. and Jarrett, J.: Comparing two contrail models under certain and uncertain inputs, AIAA SCITECH 2024 Forum, https://doi.org/10.2514/6.2024-1023, 2024.

Akhtar Martínez, C., Eastham, S. D., and Jarrett, J. P.: Contrail models lacking post-fallstreak behavior could underpredict lifetime optical depth, EGUsphere, 2025, 1–26, https://doi.org/10.5194/egusphere-2025-278, 2025.

Ramkrishna, D.: Population Balances: Theory and Applications to Particulate Systems in Engineering, Academic Press, 2000.

Schumann, U.: A contrail cirrus prediction model, Geoscientific Model Development, 5, 543–580, https://doi.org/10.5194/gmd-5-543-2012, 2012.

Fritz, T. M., Eastham, S. D., Speth, R. L., and Barrett, S. R. H.: The role of plume-scale processes in long-term impacts of aircraft emissions, Atmospheric Chemistry and Physics, 20, 5697–5727, https://doi.org/10.5194/acp-20-5697-2020, 2020.

Schumann, U., Konopka, P., Baumann, R., Busen, R., Gerz, T., Schlager, T., Schulte, P., and Volkert, H.: Estimate of diffusion parameters of aircraft exhaust plumes near the tropopause from nitric oxide and turbulence measurements, Journal of Geophysical Research, 100, D7, 147–162, 1995.

Gierens, K. M., Monier, M., and Gayet, J. F.: The deposition coefficient and its role for cirrus clouds, Journal of Geophysical Research, 108, D2, https://doi.org/10.1029/2001JD001558, 2003.

Seinfeld, J. H. and Pandis, S. N.: Atmospheric Chemistry and Physics: From Air Pollution to Climate Change, 3rd Edn., John Wiley & Sons, Hoboken, New Jersey, USA, 2016.

Xu, M., Meijer, V., Barrett, S. R. H., and Eastham, S. D.: Evaluation of the APCEMM intermediate-fidelity contrail model using LIDAR observations, Presented at the American Geophysical Union (AGU) Fall Meeting, Board 2426, 2023, https://agu.confex.com/agu/fm23/meetingapp.cgi/Paper/1443542.

Nelson, J. and Knight, C.: Snow crystal habit changes explained by layer nucleation, Journal of the Atmospheric Sciences, 55, 1452–1465, https://doi.org/10.1175/1520-0469(1998)055<1452:SCHCEB>2.0.CO;2, 1998.

Magee, N., Miller, A., Amaral, M., and Cumiskey, A.: Mesoscopic surface roughness of ice crystals pervasive across a wide range of ice crystal conditions, Atmospheric Chemistry and Physics, 14, 12357–12371, https://doi.org/10.5194/acp-14-12357-2014, 2014.

Ham, F.: Shape-preserving solutions of the time-dependent diffusion equation, Quarterly of Applied Mathematics, 17, 137–145, https://doi.org/10.1090/qam/108196, 1959.

Avramov, A. and Harrington, J. Y.: The influence of parameterized ice habit on simulated mixed-phase Arctic clouds, Journal of Geophysical Research: Atmospheres, 115, D03205, https://doi.org/10.1029/2009JD012108, 2010.

Libbrecht, K.: Growth rates of the principal facets of ice between 210 °C and 240 °C, Journal of Crystal Growth, 247, 530–540, https://doi.org/10.1016/S0022-0248(02)01996-6, 2003.

https://doi.org/10.5194/jecats-2026-12
Preprint. Discussion started: 28 July 2026

Goodman, J., Pueschel, R. F., Jensen, E. J., Verma, S., Ferry, G. V., Howard, S. D., Kinne, S. A., and Baumgardner, D.: Shape and size of contrail ice particles, Geophysical Research Letters, 25, 1327–1330, 1998.

Yang, P., Hong, G., Dessler, A. E., Ou, S. S., Liou, K. N., Minnis, P., and Harshvardhan: Contrails and induced cirrus: Optics and radiation, Bulletin of the American Meteorological Society, 91, 4, 473–478, https://doi.org/10.1175/2009BAMS2837.1, 2010.

Intergovernmental Panel on Climate Change (IPCC), Penner, J. E., Lister, D. H., Griggs, D. J., Dokken, D. J., and McFarland, M. (Eds.): Aviation and the Global Atmosphere, Special Report, Cambridge University Press, Cambridge, UK, 373 pp., Scientific Assessment Panel to the Montreal Protocol on Substances that Deplete the Ozone Layer, 1999, https://www.grida.no/climate/ipcc/aviation/038.htm.

Iwabuchi, H., Yang, P., Liou, K. N., and Minnis, P.: Physical and optical properties of persistent contrails: Climatology and interpretation, Journal of Geophysical Research: Atmospheres, 117, D06215, https://doi.org/10.1029/2011JD017020, 2012.

Krämer, M., Rolf, C., Spelten, N., Afchine, A., Fahey, D., Jensen, E., Khaykin, S., Kuhn, T., Lawson, P., Lykov, A., Pan, L. L., Riese, M., Rollins, A., Stroh, F., Thornberry, T., Wolf, V., Woods, S., Spichtinger, P., Quaas, J., and Sourdeval, O.: A microphysics guide to cirrus – Part 2: Climatologies of clouds and humidity from observations, Atmospheric Chemistry and Physics, 20, 12569–12608, https://doi.org/10.5194/acp-20-12569-2020, 2020.

Wolf, K., Bellouin, N., and Boucher, O.: Radiative effect by cirrus cloud and contrails – A comprehensive sensitivity study, EGUsphere [preprint], https://doi.org/10.5194/egusphere-2023-155, 2023.

Kärcher, B.: Formation and radiative forcing of contrail cirrus, Nature Communications, 9, 1824, https://doi.org/10.1038/s41467-018-04068-0, 2018.

Jones, H. M., Haywood, J., Marenco, F., Forster, P., Highwood, J., Meyer, J., Kärcher, B., Schlager, H., Petzold, A., Baumgardner, D., Gierens, K., Busen, R., Dörnbrack, A., and MacKenzie, A. R.: A methodology for in-situ and remote sensing of microphysical and radiative properties of contrails as they evolve into cirrus, Atmospheric Chemistry and Physics, 12, 8157–8175, https://doi.org/10.5194/acp-12-8157-2012, 2012.

Heymsfield, A. J., Lawson, R. P., and Sachse, G. W.: Growth of ice crystals in a precipitating contrail, Geophysical Research Letters, 25, 1335–1338, https://doi.org/10.1029/98GL00189, 1998.

Schumann, U., Baumann, R., Baumgardner, D., Bedka, S. T., Duda, D. P., Freudenthaler, V., Gayet, J.-F., Heymsfield, A. J., Minnis, P., Quante, M., Raschke, E., Schlager, H., Vázquez-Navarro, M., Voigt, C., and Wang, Z.: Properties of individual contrails: a compilation of observations and some comparisons, Atmospheric Chemistry and Physics, 17, 403–438, https://doi.org/10.5194/acp-17-403-2017, 2017.

Sussmann, R.: Optical properties of contrail-induced cirrus: discussion of unusual halo phenomena, Applied Optics, 36, 4195–4201, https://doi.org/10.1364/AO.36.004195, 1997.

Stout, J. E., Arya, S. P., and Genikhovich, E. L.: The Effect of Nonlinear Drag on the Motion and Settling Velocity of Heavy Particles in a Turbulent Atmosphere, Journal of the Atmospheric Sciences, 52, 3836–3848, https://doi.org/10.1175/1520-0469(1995)052<3836:TEONDO>2.0.CO;2, 1995.

Chen, X., Liu, Z., Chen, Y., and Wang, H.: Analytical expression for predicting the reduced settling velocity of small particles in turbulence, Environmental Fluid Mechanics, 20, 905–922, https://doi.org/10.1007/s10652-019-09731-8, 2020.

Akutina, Y., Revil-Baudard, T., Chauchat, J., and Eiff, O.: Experimental evidence of settling retardation in a turbulence column, Physical Review Fluids, 5, 014303, https://doi.org/10.1103/PhysRevFluids.5.014303, 2020.

https://doi.org/10.5194/jecats-2026-12
Preprint. Discussion started: 28 July 2026

Fornari, W., Picano, F., Sardina, G., and Brandt, L.: Reduced particle settling speed in turbulence, Journal of Fluid Mechanics, 808, 153–167, https://doi.org/10.1017/jfm.2016.648, 2016.

Pruppacher, H. R. and Klett, J. D.: Microphysics of Clouds and Precipitation, Kluwer Academic Publishers, Dordrecht, Netherlands, 2nd edition, ISBN 978-0-7923-4211-3, 1997.

Breit, F., Jakobsen, H. A., and von Harbou, E.: Formulation of a mass-based population balance equation: insights into derivation, mass transfer, and nondimensionalization, Chemical Engineering Communications, 212, 999–1012, https://doi.org/10.1080/00986445.2024.2445228, 2025.

Guignery, F., Montreuil, E., Thual, O., and Vancassel, X.: Contrail microphysics in the near wake of a realistic wing through RANS simulations, Aerospace Science and Technology, 23, 399–408, https://doi.org/10.1016/j.ast.2011.09.011, 2012.

Montreuil, E., Ghedhaifi, W., Chmielaski, V., Vuillot, F., Gand, F., and Loseille, A.: Numerical Simulation of contrail formation on the Common Research Model wing/body/engine configuration, in: 2018 Atmospheric and Space Environments Conference, https://doi.org/10.2514/6.2018-3189, 2018.

Lewellen, D. C.: A Large-Eddy Simulation Study of Contrail Ice Number Formation, Journal of the Atmospheric Sciences, 77, 2585–2604, https://doi.org/10.1175/JAS-D-19-0322.1, 2020.

Bouhafid, Y., Bonne, N., and Jacquin, L.: Combined Reynolds-averaged Navier-Stokes/Large-Eddy Simulations for an aircraft wake until dissipation regime, Aerospace Science and Technology, 154, 109512, https://doi.org/10.1016/j.ast.2024.109512, 2024.

Chen, J.-P. and Lamb, D.: The Theoretical Basis for the Parameterization of Ice Crystal Habits: Growth by Vapor Deposition, Journal of Atmospheric Sciences, 51, 1206–1222, https://doi.org/10.1175/1520-0469(1994)051<1206:TTBFTP>2.0.CO;2, 1994.

Nelson, J. T. and Baker, M. B.: New theoretical framework for studies of vapor growth and sublimation of small ice crystals in the atmosphere, Journal of Geophysical Research: Atmospheres, 101, 7033–7047, https://doi.org/10.1029/95JD03162, 1996.

Zhang, C. and Harrington, J. Y.: Including Surface Kinetic Effects in Simple Models of Ice Vapor Diffusion, Journal of the Atmospheric Sciences, 71, 372–390, https://doi.org/10.1175/JAS-D-13-0103.1, 2014.

Harrington, J. Y., Sokolowsky, G. A., and Morrison, H.: Semianalytic Functions to Calculate the Deposition Coefficients for Ice Crystal Vapor Growth in Bin and Bulk Microphysical Models, Journal of the Atmospheric Sciences, 78, 1735–1752, https://doi.org/10.1175/JAS-D-20-0307.1, 2021.

Laurencin, C. N., Didlake, A. C., Harrington, J. Y., and Jensen, A. A.: Evaluating an Ice Crystal Trajectory Growth (ICTG) Model on a Quasi-Idealized Simulation of a Squall Line, Journal of Advances in Modeling Earth Systems, 14, e2021MS002764, https://doi.org/10.1029/2021MS002764, 2022.

Harrington, J. Y., Moyle, A., Hanson, L. E., and Morrison, H.: On Calculating Deposition Coefficients and Aspect-Ratio Evolution in Approximate Models of Ice Crystal Vapor Growth, Journal of the Atmospheric Sciences, 76, 1609–1625, https://doi.org/10.1175/JAS-D-18-0319.1, 2019.

Harrington, J. Y. and Pokrifka, G. F.: An Approximate Criterion for Morphological Transformations in Small Vapor Grown Ice Crystals, Journal of the Atmospheric Sciences, 81, 401–416, https://doi.org/10.1175/JAS-D-23-0131.1, 2024.

Bailey, M. and Hallett, J.: Laboratory Measured Ice Crystal Capacitances and Mass Dimensional Relations, 13th Conference on Cloud Physics, American Meteorological Society, Poster P1.30, 2010.

https://doi.org/10.5194/jecats-2026-12
Preprint. Discussion started: 28 July 2026

Bailey, M. P. and Hallett, J.: A Comprehensive Habit Diagram for Atmospheric Ice Crystals: Confirmation from the Laboratory, AIRS II, and Other Field Studies, Journal of the Atmospheric Sciences, 66, 2888–2899, https://doi.org/10.1175/2009JAS2883.1, 2009.

Kuroda, T. and Lacmann, R.: Growth kinetics of ice from the vapour phase and its growth forms, Journal of Crystal Growth, 56, 189–205, https://doi.org/10.1016/0022-0248(82)90028-8, 1982.

Westbrook, C. D., Hogan, R. J., Field, P. R., Illingworth, A. J., and Blackman, T. M.: The Capacitance of Pristine Ice Crystals and Aggregate Snowflakes, Journal of the Atmospheric Sciences, 65, 206–219, https://doi.org/10.1175/2007JAS2315.1, 2008.

Murphy, D. M. and Koop, T.: Review of the vapour pressures of ice and supercooled water for atmospheric applications, Quarterly Journal of the Royal Meteorological Society, 131, 1539–1565, https://doi.org/10.1256/qj.04.94, 2005.

Li, J., Kim, J.-H., Sridhar, B., and Ng, H. K.: Ames Contrail Simulation Model: Modeling Aviation Induced Contrails and the Computation of Contrail Radiative Forcing Using Air Traffic Data, NASA Technical Memorandum, NASA/TM–202300014633, NASA Langley Research Center, https://ntrs.nasa.gov/citations/20230014633, 2023.

Unterstrasser, S. and Gierens, K.: Numerical simulations of contrail-to-cirrus transition – Part 1: An extensive parametric study, Atmospheric Chemistry and Physics, 10, 2017–2036, https://doi.org/10.5194/acp-10-2017-2010, 2010.

Unterstrasser, S. and Gierens, K.: Numerical simulations of contrail-to-cirrus transition – Part 2: Impact of initial ice crystal number, radiation, stratification, secondary nucleation and layer depth, Atmospheric Chemistry and Physics, 10, 2037–2051, https://doi.org/10.5194/acp-10-2037-2010, 2010.

Unterstrasser, S., Gierens, K., Sölch, I., and Lainer, M.: Numerical Simulations of Homogeneously Nucleated Natural Cirrus and Contrail-Cirrus. Part 1: How Different Are They?, Meteorologische Zeitschrift, 26, 621–642, https://doi.org/10.1127/metz/2016/0777, 2017.

Unterstrasser, S., Gierens, K., Sölch, I., and Wirth, M.: Numerical Simulations of Homogeneously Nucleated Natural Cirrus and Contrail-Cirrus. Part 2: Interaction on Local Scale, Meteorologische Zeitschrift, 26, 643–661, https://doi.org/10.1127/metz/2016/0780, 2017.

Ganser, G. H.: A rational approach to drag prediction of spherical and nonspherical particles, Powder Technology, 77, 2, 143–152, 1993.

Nielsen, P.: Turbulence effects on the settling of suspended particles, Journal of Sedimentary Petrology, 63, 5, 835–838, 1993.

Buongiorno, J.: Convective transport in nanofluids, Journal of Heat Transfer, 128, 3, 240–250, https://doi.org/10.1115/1.2150834, 2006.

Jafarimoghaddam, A., Turkyilmazoglu, M., Roşca, A. V., and Pop, I.: Complete theory of the elastic wall jet: A new flow geometry with revisited two-phase nanofluids, European Journal of Mechanics - B/Fluids, 86, 25–36, https://doi.org/10.1016/j.euromechflu.2020.11.006, 2021.

Brennen, C. E.: Fundamentals of Multiphase Flow, Cambridge University Press, https://doi.org/10.1017/CBO9780511807169, 2005.

Kaveh, K. and Malcherek, A.: Settling velocity characteristics of inertial particles in turbulent and wave-induced environments, International Journal of Multiphase Flow, 179, 104930, https://doi.org/10.1016/j.ijmultiphaseflow.2024.104930, 2024.

Xu, M.: Development and evaluation of contrail models, PhD thesis, Massachusetts Institute of Technology, https://dspace.mit.edu/handle/1721.1/155484, 2024.

https://doi.org/10.5194/jecats-2026-12
Preprint. Discussion started: 28 July 2026

J. N. Welss, C. Siewert, and A. Seifert, Explicit Habit-Prediction in the Lagrangian Super-Particle Ice Microphysics Model McSnow, Journal of Advances in Modeling Earth Systems, vol. 16, no. 4, 2024.

A. J. Heymsfield, S. Lewis, A. Bansemer, J. Iaquinta, L. M. Miloshevich, M. Kajikawa, C. Twohy, and M. R. Poellot, A General Approach for Deriving the Properties of Cirrus and Stratiform Ice Cloud Particles, Journal of the Atmospheric Sciences, vol. 59, no. 1, pp. 3–29, 2002.

D. C. Lewellen, O. Meza, and W. W. Huebsch, Persistent Contrails and Contrail Cirrus. Part I: Large-Eddy Simulations from Inception to Demise, Journal of the Atmospheric Sciences, vol. 71, no. 12, pp. 4399–4419, 2014.

M. Bailey and J. Hallett, Growth Rates and Habits of Ice Crystals between -20° and -70°C, Journal of the Atmospheric Sciences, vol. 61, no. 5, pp. 514–544, 2004.

Appendix

Appendix A: Derivation of Moment Equations from the Population Balance Equation

In this section, we derive the macroscopic advection–diffusion equations (ADEs) for the number and mass concentrations of ice particles from the Population Balance Equation (PBE).

A1 Population Balance Equation (PBE)

The PBE for the distribution function $f(\mathbf{x},m,t)$ is given by:

$$\frac{\partial f}{\partial t} + \nabla\cdot(\mathbf{v}_p f) = -\frac{\partial}{\partial m}\Big(\dot{m}\, f\Big) + \nabla\cdot\Big(\tilde{\mathcal{D}}\,\nabla f\Big) + S_f, \tag{A1}$$

where, $\mathbf{v}_p(\mathbf{x},t)$ is the particle bulk velocity, defined as:

$$\mathbf{v}_p = \mathbf{v}_{slp} + \underbrace{(w_x,w_y,w_z)^\top}_{\substack{\text{background velocity}\\ \text{(wind components)}}} \approx (0,0,v_s)^\top + \underbrace{(w_x,w_y,w_z)^\top}_{\text{background velocity}} = (w_x,w_y,w_z+v_s)^\top. \tag{A2}$$

In Eq. (A2), $\mathbf{v}_{slp}$ denotes the bulk slip velocity of the particle phase within a fluid undergoing turbulent mixing.

In addition, $\dot{m} = \rho_{\text{dep}}\, f_{\mathcal{V}}(m,\mathbf{x},t)$ is the particle growth rate, $\tilde{\mathcal{D}}(\mathbf{x},t,c_N,m)$ is the diffusion coefficient, and $S_f(\mathbf{x},m,t)$ represents source/sink terms. Since the particle mass distribution is narrowly peaked, under the monodisperse assumption, at a representative mass $\bar{m}(\mathbf{x},t)$, hence $f(\mathbf{x},m,t) = c_N(\mathbf{x},t)\,\delta\Big(m-\bar{m}(\mathbf{x},t)\Big)$, where $c_N(\mathbf{x},t)$ is the particle number concentration. Therefore, we can write: $f_{\mathcal{V}}(m,\mathbf{x},t) \approx f_{\mathcal{V}}(\bar{m}(\mathbf{x},t),\mathbf{x},t)$, $\tilde{\mathcal{D}}(\mathbf{x},m,t,c_N) \approx \tilde{\mathcal{D}}(\mathbf{x},\bar{m}(\mathbf{x},t),t,c_N)$, and $\mathbf{v}_p(\mathbf{x},m,t) \approx \mathbf{v}_p(\mathbf{x},\bar{m}(\mathbf{x},t),t)$.

The number and mass concentrations are defined by:

$$c_N(\mathbf{x},t) = \int_0^\infty f(\mathbf{x},m,t)\,dm, \quad c_M(\mathbf{x},t) = \int_0^\infty m\, f(\mathbf{x},m,t)\,dm. \tag{A3}$$

https://doi.org/10.5194/jecats-2026-12
Preprint. Discussion started: 28 July 2026

Using the monodisperse assumption, we obtain:

$$c_N(\mathbf{x},t) = c_N(\mathbf{x},t), \quad c_M(\mathbf{x},t) = \bar{m}(\mathbf{x},t)\, c_N(\mathbf{x},t). \tag{A4}$$

A2 Derivation of the Zeroth Moment Equation

Integrating the PBE (A1) over m:

$$\begin{aligned}
&\int_0^\infty \left\{ \frac{\partial f}{\partial t} + \nabla \cdot (\mathbf{v}_p f) \right\} dm = \int_0^\infty \left\{ -\frac{\partial}{\partial m}(\dot{m} f) + \nabla \cdot (\tilde{\mathcal{D}} \nabla f) + S_f \right\} dm \;\Rightarrow \\
&\frac{\partial}{\partial t}\int_0^\infty f\, dm + (\nabla \cdot \mathbf{v}_p) \int_0^\infty f\, dm + \mathbf{v}_p \cdot \nabla \int_0^\infty f\, dm = -\left[\dot{m} f\right]_0^\infty + \nabla \cdot \left(\tilde{\mathcal{D}} \nabla \int_0^\infty f\, dm\right) \;\Rightarrow \\
&\frac{\partial c_N}{\partial t} + \nabla \cdot \left(\mathbf{v}_p c_N\right) = \nabla \cdot \left(\tilde{\mathcal{D}} \nabla c_N\right) + S_{c_N}
\end{aligned} \tag{A5}$$

where $S_{c_N}(\mathbf{x},t) = \int_0^\infty S_f(\mathbf{x},m,t)\, dm$. Notably, the boundary term $[\dot{m} f]_0^\infty$ cancels out since there is no particle distribution at $m = 0$ or as $m \to \infty$.

A3 Derivation of the First Moment Equation

Multiplying the PBE by m and integrating over m:

$$\begin{aligned}
&\int_0^\infty m \left\{ \frac{\partial f}{\partial t} + \nabla \cdot (\mathbf{v}_p f) \right\} dm = \int_0^\infty m \left\{ -\frac{\partial}{\partial m}(\dot{m} f) + \nabla \cdot (\tilde{\mathcal{D}} \nabla f) + S_f \right\} dm \;\Rightarrow \\
&\frac{\partial}{\partial t}\int_0^\infty m\, f\, dm + (\nabla \cdot \mathbf{v}_p) \int_0^\infty m\, f\, dm + \mathbf{v}_p \cdot \nabla \int_0^\infty m\, f\, dm = \\
&-\left[m\, \dot{m} f\right]_0^\infty + \int_0^\infty \dot{m}\, f\, dm + \nabla \cdot \left(\tilde{\mathcal{D}} \nabla \int_0^\infty m\, f\, dm\right) \;\Rightarrow \\
&\frac{\partial c_M}{\partial t} + \nabla \cdot \left(\mathbf{v}_p c_M\right) = \nabla \cdot \left(\tilde{\mathcal{D}} \nabla c_M\right) + \rho_{dep}\, f_{\mathcal{V}}\left(\bar{m}(\mathbf{x},t), \mathbf{x}, t\right) c_N(\mathbf{x},t) + S_{c_M}.
\end{aligned} \tag{A6}$$

where $S_{c_M}(\mathbf{x},t) = \int_0^\infty m\, S_f(\mathbf{x},m,t)\, dm$.

A4 Derivation of the Per-Particle Mass Evolution Equation

In previous sections, the representative ice-particle mass was denoted by $\bar{m}$; here, by slight abuse of notation we write m for the same quantity. We omit all source terms except the growth term $\rho_{\text{dep}}\, f_{\mathcal{V}}$ in the c_M equation.

https://doi.org/10.5194/jecats-2026-12
Preprint. Discussion started: 28 July 2026

Under monodispersity, we have $m = \frac{c_M}{c_N}$. Combining the two moments, we write:

$$\left[\frac{\partial c_M}{\partial t} + \nabla\cdot(\mathbf{v}_p c_M)\right] - m\left[\frac{\partial c_N}{\partial t} + \nabla\cdot(\mathbf{v}_p c_N)\right]$$
$$= \nabla\cdot\left(\tilde{\mathcal{D}}\nabla c_M\right) - m\nabla\cdot\left(\tilde{\mathcal{D}}\nabla c_N\right) + \rho_{dep} f_{\mathcal{V}} c_N. \tag{A7}$$

Since:

$$\frac{\partial(c_N m)}{\partial t} = m\frac{\partial c_N}{\partial t} + c_N\frac{\partial m}{\partial t}, \tag{A8}$$

$$\nabla\cdot(\mathbf{v}_p m c_N) = c_N \mathbf{v}_p\cdot\nabla m + m\mathbf{v}_p\cdot\nabla c_N + m c_N \nabla\cdot\mathbf{v}_p, \tag{A9}$$

the m-weighted terms cancel upon subtraction and the left-hand side reduces to:

$$c_N\left(\frac{\partial m}{\partial t} + \mathbf{v}_p\cdot\nabla m\right) = c_N\frac{\mathrm{D}m}{\mathrm{D}t}. \tag{A10}$$

Thus:

$$c_N\frac{\mathrm{D}m}{\mathrm{D}t} = \nabla\cdot\left(\tilde{\mathcal{D}}\nabla(c_N m)\right) - m\nabla\cdot\left(\tilde{\mathcal{D}}\nabla c_N\right) + \rho_{dep} f_v c_N. \tag{A11}$$

Moreover, we have:

$$\nabla(c_N m) = c_N\nabla m + m\nabla c_N, \qquad \nabla^2(c_N m) = c_N\nabla^2 m + 2\nabla m\cdot\nabla c_N + m\nabla^2 c_N. \tag{A12}$$

Therefore, expanding the diffusion difference gives:

$$\nabla\cdot\left(\tilde{\mathcal{D}}\nabla(c_N m)\right) - m\nabla\cdot\left(\tilde{\mathcal{D}}\nabla c_N\right)$$
$$= \tilde{\mathcal{D}}\left(c_N\nabla^2 m + 2\nabla m\cdot\nabla c_N + m\nabla^2 c_N\right) + (\nabla\tilde{\mathcal{D}})\cdot(c_N\nabla m + m\nabla c_N)$$
$$- m\left(\tilde{\mathcal{D}}\nabla^2 c_N + (\nabla\tilde{\mathcal{D}})\cdot\nabla c_N\right)$$
$$= c_N\left[\tilde{\mathcal{D}}\nabla^2 m + (\nabla\tilde{\mathcal{D}})\cdot\nabla m\right] + 2\tilde{\mathcal{D}}\nabla m\cdot\nabla c_N. \tag{A13}$$

Hence, using $\tilde{\mathcal{D}}\nabla^2 m + (\nabla\tilde{\mathcal{D}})\cdot\nabla m = \nabla\cdot(\tilde{\mathcal{D}}\nabla m)$ the per-particle evolution equation in material form is written as:

$$\frac{\partial m}{\partial t} + \mathbf{v}_p\cdot\nabla m = \nabla\cdot\left(\tilde{\mathcal{D}}\nabla m\right) + \frac{2\tilde{\mathcal{D}}}{c_N}\nabla m\cdot\nabla c_N + \rho_{\mathrm{dep}} f_{\mathcal{V}}. \tag{A14}$$

https://doi.org/10.5194/jecats-2026-12
Preprint. Discussion started: 28 July 2026

Appendix B: Derivation of the Particle-Phase Momentum Equation

In multiphase flow modeling, the Euler–Euler framework treats both the fluid and particulate phases as interpenetrating continua. To better conceptualize this, consider the particle phase settling within a fluid subject to turbulent mixing. Since the mean fluid motion (i.e., wind components) is already incorporated into the definition of $\mathbf{v}_p$, the fluid velocity appearing in the slip velocity $\mathbf{v}_{\mathrm{slp}}$ accounts only for turbulent fluctuations. Under this setup, the full momentum equation for the particle phase takes the following form Brennen (2005):

$$\frac{\partial(\epsilon_p\rho_p\mathbf{v}_{slp})}{\partial t}+\nabla\cdot\left(\epsilon_p\rho_p\,\mathbf{v}_{slp}\mathbf{v}_{slp}\right)=-\epsilon_p\nabla p+\nabla\cdot\tau_p+\epsilon_p\rho_p\,\mathbf{g}+F_d, \tag{B1}$$

where ϵ_p is the particle volume fraction, ρ_p is the particle density, $\mathbf{v}_{slp}$ is the particle bulk slip velocity, p is the pressure due to the fluid phase, τ_p is the particle-phase stress tensor (namely deviatoric steress emerging on the exterior of the control volume), $\mathbf{g}$ is the gravitational acceleration vector, and F_d is the net force per unit volume acting on the particles in the control volume. In many closures the net force is modeled as proportional to ϵ_p (e.g., arising from the per-particle contribution multiplied by the local particle concentration, i.e., $F_d=\epsilon_p\,f_d$ where f_d is the average net force experienced by individual particles which is inherently different from the drag force experienced by a single settling particle in an unbounded domain). Local mechanical equilibrium $p_p=p_f$ is assumed, so that the pressure gradient acting on the particle phase is $-\epsilon_p\nabla p$. The stress tensor can be expressed as: $\tau_p=\epsilon_p\,\mu_{t,p}(\nabla\mathbf{v}_{slp}+\nabla\mathbf{v}_{slp}^{\top})$.

Expanding the LHS of Eq. (B1), we write:

$$\begin{aligned}&\frac{\partial(\epsilon_p\rho_p\mathbf{v}_{slp})}{\partial t}+\nabla\cdot\left(\epsilon_p\rho_p\,\mathbf{v}_{slp}\mathbf{v}_{slp}\right)\\&=\rho_p\mathbf{v}_{slp}\frac{\partial\epsilon_p}{\partial t}+\epsilon_p\rho_p\frac{\partial\mathbf{v}_{slp}}{\partial t}+\rho_p\mathbf{v}_{slp}\nabla\cdot(\epsilon_p\,\mathbf{v}_{slp})+\epsilon_p\rho_p(\mathbf{v}_{slp}\cdot\nabla)\mathbf{v}_{slp}\\&=\rho_p\mathbf{v}_{slp}\underbrace{\left[\frac{\partial\epsilon_p}{\partial t}+\nabla\cdot(\epsilon_p\,\mathbf{v}_{slp})\right]}_{\substack{\text{continuity equation of}\\\text{the particle phase}}}+\epsilon_p\rho_p\left[\frac{\partial\mathbf{v}_{slp}}{\partial t}+(\mathbf{v}_{slp}\cdot\nabla)\mathbf{v}_{slp}\right].\end{aligned} \tag{B2}$$

For the stress term, we write:

$$\frac{1}{\epsilon_p\rho_p}\nabla\cdot\tau_p=\frac{\nu_t}{\epsilon_p}\nabla\cdot[\epsilon_p(\nabla\mathbf{v}_{slp}+\nabla\mathbf{v}_{slp}^{\top})]=\nu_t\left[\nabla^2\mathbf{v}_{slp}+\frac{1}{\epsilon_p}(\nabla\epsilon_p\cdot\nabla)\mathbf{v}_{slp}+\frac{1}{\epsilon_p}(\nabla\epsilon_p\cdot\nabla)^{\top}\mathbf{v}_{slp}\right] \tag{B3}$$

where $\nu_t:=\frac{\mu_{t,p}}{\rho_p}$ is the average turbulent eddy-viscosity.

Substituting the stress term into Eq. (B1) and invoking the first moment equation, Eq. (A6), to represent particle-phase continuity, where $c_M=\rho_{\mathrm{dep}}\,\epsilon_p=\rho_p\,\epsilon_p$, $\nabla\cdot\mathbf{v}_{\mathrm{slp}}\approx 0$, and no additional particle injection is assumed (i.e., $S_{c_M}=0$),

https://doi.org/10.5194/jecats-2026-12
Preprint. Discussion started: 28 July 2026

while also noting that the advection term has been replaced with $\mathbf{v}_{\mathrm{slp}}$, we obtain:

$$\frac{\partial \mathbf{v}_{slp}}{\partial t} + (\mathbf{v}_{slp}\cdot\nabla)\mathbf{v}_{slp} = \nu_t\Big[\nabla^2\mathbf{v}_{slp} + \tfrac{1}{\epsilon_p}(\nabla\epsilon_p\cdot\nabla)\mathbf{v}_{slp} + \tfrac{1}{\epsilon_p}(\nabla\epsilon_p\cdot\nabla)^\top\mathbf{v}_{slp}\Big] - \frac{\nabla p}{\rho_p} + \mathbf{g} + \frac{f_d}{\rho_p} - \frac{\mathbf{v}_{slp}}{\epsilon_p}\Big[\nabla\cdot\Big(\tilde{\mathcal{D}}\nabla\epsilon_p\Big) + f_v\big(\bar{m}(\mathbf{x},t),\mathbf{x},t\big)\,c_N(\mathbf{x},t)\Big]. \tag{B4}$$

In general, the above equation is coupled with the fluid phase through the pressure and force terms, and with the first and second moments of the particle distribution. Notably, as f_d approaches the drag force on a single settling particle in an unbounded domain, the pressure gradient tends toward the hydrostatic condition, $\nabla p = \rho_f\mathbf{g}$.

The above equation can be written as:

$$\frac{\partial \mathbf{v}_{slp}}{\partial t} + (\mathbf{v}_{slp}\cdot\nabla)\mathbf{v}_{slp} = \nu_t\nabla^2\mathbf{v}_{slp} + \boldsymbol{C}_f + \boldsymbol{C}_{c_M,c_N,f_v}. \tag{B5}$$

where $\boldsymbol{C}_f$ represents the coupling between $\mathbf{v}_{slp}$ and the fluid phase, and is expressed as $\boldsymbol{C}_f = -\frac{\nabla p}{\rho_p} + \mathbf{g} + \frac{f_d}{\rho_p}$; and $\boldsymbol{C}_{c_M,c_N,f_v}$ captures the coupling of $\mathbf{v}_{slp}$ to the mass and number concentration fields, as well as to the growth term, and is given by $\boldsymbol{C}_{c_M,c_N,f_v} = -\frac{\mathbf{v}_{slp}}{\epsilon_p}\big[\nabla\cdot\Big(\tilde{\mathcal{D}}\nabla\epsilon_p\Big) + f_v\big(\bar{m}(\mathbf{x},t),\mathbf{x},t\big)\,c_N(\mathbf{x},t)\big] + \nu_t\Big[\frac{1}{\epsilon_p}(\nabla\epsilon_p\cdot\nabla)\mathbf{v}_{slp} + \frac{1}{\epsilon_p}(\nabla\epsilon_p\cdot\nabla)^\top\mathbf{v}_{slp}\Big]$.

Accurate solution of the above equation presents formidable challenges in (i) specifying boundary and initial conditions, (ii) coupling the evolving fluid phase with particle number and mass concentrations, and (iii) incorporating microphysical growth rates. In addition, in practice, the eddy viscosity is not only space- and time-dependent, but also anisotropic-varying across different spatial directions.

A Compressed Low-Order Model

The above equation can be expressed solely in terms of the particle bulk settling velocity v_s in the z-direction by collapsing the turbulent-mixing in the vertical dimension. In other words, the 'quasi-hovering' (*loitering*) behavior of horizontally distributed particles can be interpreted as an effective turbulent mixing in the vertical direction. For this reason, this type of 1D modeling is referred to as a *compressed low-order model*.

This framework motivates defining an effective vertical eddy viscosity, $\nu_{\mathbf{t,ef}} \approx \langle\nu_t(x,y,z)\rangle$, which encapsulates the total turbulent mixing effect.

Here, we assume that the particle bulk velocity is initially zero at a reference plane, $z_{\mathbf{ref}}$, and remains negligible for an extended period due to strong early-time turbulent mixing effect when the concentration field is at its maximum. Far below $z_{\mathbf{ref}}$, the local concentration decreases, and particle growth amplifies gravitational settling. This leads to an increase in both the Galileo and Stokes numbers. Consequently, the bulk net force f_d asymptotically converges to the drag force experienced by an individual particle in an unbounded domain, and the pressure gradient approaches hydrostatic balance, $\nabla p = \rho_f\mathbf{g}$.

Under this framework, the fluid coupling term $\boldsymbol{C}_f$ is encoded within the boundary conditions, and, for simplicity, the term representing coupling to the concentration field, $\boldsymbol{C}_{c_M,c_N,f_v}$, is not explicitly accounted for. However, since

https://doi.org/10.5194/jecats-2026-12
Preprint. Discussion started: 28 July 2026

the present bulk settling model is coupled to the microphysical ADEs, the particle growth term is implicitly included, as the growth makes $v_{\mathbf{ter}} := v_{\mathbf{ter}}(z,t)$.

Within this framework, the fluid coupling term $\boldsymbol{C}_f$ is encoded within the boundary conditions. For simplicity, the coupling term associated with the concentration field, $\boldsymbol{C}_{c_M,c_N,f_v}$, is neglected. Nonetheless, because the bulk settling model is coupled to the microphysical ADEs, the effects of particle growth are implicitly represented through the time dependence of the terminal velocity, $v_{\mathbf{ter}} := v_{\mathbf{ter}}(z,t)$. Therefore, with appropriately chosen boundary conditions, Eq. (B5) reduces to the following 1D model:

$$\frac{\partial v_s}{\partial t} + v_s \frac{\partial v_s}{\partial z} = \nu_{\mathbf{t,ef}} \frac{\partial^2 v_s}{\partial z^2}, \quad v_s(z_{\mathbf{ref}}, t=0) = 0, \quad v_s(z \ll z_{\mathbf{ref}}, t=0) = v_{\mathbf{ter}}, \quad \lim_{t\to\infty} v_s = v_{\mathbf{ter}}. \tag{B6}$$

where $v_{\mathbf{ter}}$ denotes the conventional terminal velocity of individual particles in an unbounded domain. Notably, by prescribing $v_{\mathbf{ter}}$ as the outer boundary condition, the model inherently captures the interplay between (i) turbulent mixing in the highly concentrated upper region (*loitering*), (ii) the transition of the bulk net force f_d into the drag force on individual particles, and (iii) the acceleration of this transition by micro-physical growth processes.

In addition, by expressing the asymptotic settling velocity as $\lim_{t\to\infty} v_s = \alpha v_{\mathbf{ter}}$, where $\alpha \propto \mathrm{St}$ or Ga, the model more accurately captures the *sweeping* mechanism. By allowing α to exceed unity in inertia-dominated regimes, this formulation can represent the increased settling velocity associated with the *sweeping* mechanism.

Appendix C: Closed-Form Solution for the Bulk Settling Velocity $v_s(z,t)$

Employing the Cole–Hopf transformation,

$$\hat{v}_s(z,t) = -2\nu_{\mathbf{t,ef}} \frac{\partial}{\partial z} \ln \varphi(z,t) = -2\nu_{\mathbf{t,ef}} \frac{\frac{\partial \varphi}{\partial z}}{\varphi}. \tag{C1}$$

where φ satisfies the linear heat equation:

$$\frac{\partial \varphi}{\partial t} = \nu_{\mathbf{t,ef}} \frac{\partial^2 \varphi}{\partial z^2}. \tag{C2}$$

with the initial condition $\varphi(z,0) =: \varphi_0(z)$ as:

$$\varphi_0(z) = \exp\Big(-\frac{1}{2\nu_{\mathbf{t,ef}}} \int_{z_{\mathbf{relax}}}^{z} \hat{v}_s(\xi,0)\, d\xi\Big) = \begin{cases} \exp\big(-\frac{v_{\mathbf{ter}}}{2\nu_{\mathbf{t,ef}}}(z - z_{\mathbf{relax}})\big), & z \le z_{\mathbf{relax}}, \\ 1, & z > z_{\mathbf{relax}}. \end{cases} \tag{C3}$$

The solution of the heat equation with initial data φ_0 is given by convolution with the heat kernel:

$$G(\xi,t) = \frac{1}{\sqrt{4\pi\nu_{\mathbf{t,ef}} t}} \exp\Big(-\frac{\xi^2}{4\nu_{\mathbf{t,ef}} t}\Big), \qquad t > 0, \tag{C4}$$

https://doi.org/10.5194/jecats-2026-12
Preprint. Discussion started: 28 July 2026

so for $t > 0$

$$\varphi(z,t) = \int_{-\infty}^{\infty} G(z-y,t)\,\varphi_0(y)\,dy. \tag{C5}$$

845 Splitting the integral at $y = z_{\mathbf{relax}}$, and setting $\Delta_0 := z - z_{\mathbf{relax}}$, we write:

$$\varphi(z,t) = \int_{-\infty}^{z_{\mathbf{relax}}} G(z-y,t)\,e^{-\frac{v_{\mathbf{ter}}}{2\nu_{\mathbf{t,ef}}}(y-z_{\mathbf{relax}})}\,dy \;+\; \int_{z_{\mathbf{relax}}}^{\infty} G(z-y,t)\,dy =: I_1 + I_2. \tag{C6}$$

I_2 can be computed as:

$$I_2 = \frac{1}{\sqrt{4\pi\nu_{\mathbf{t,ef}}t}} \int_{z_{\mathbf{relax}}}^{\infty} \exp\Big(-\frac{(z-y)^2}{4\nu_{\mathbf{t,ef}}t}\Big)\,dy = \frac{1}{2}\Big(1+\operatorname{erf}\Big(\frac{\Delta_0}{2\sqrt{\nu_{\mathbf{t,ef}}t}}\Big)\Big). \tag{C7}$$

For I_1, we define $s := y - z_{\text{relax}}$ so $s \in (-\infty, 0]$. Thus:

850 $$I_1 = \frac{1}{\sqrt{4\pi\nu_{\mathbf{t,ef}}t}} \int_{-\infty}^{0} \exp\Big(-\frac{(\Delta_0 - s)^2}{4\nu_{\mathbf{t,ef}}t} - \frac{v_{\mathbf{ter}}}{2\nu_{\mathbf{t,ef}}}s\Big)\,ds. \tag{C8}$$

which can be written as:

$$\begin{aligned} I_1 &= \exp\Big(\frac{v_{\mathbf{ter}}^2 t}{4\nu_{\mathbf{t,ef}}} - \frac{v_{\mathbf{ter}}\Delta_0}{2\nu_{\mathbf{t,ef}}}\Big)\cdot\frac{1}{\sqrt{4\pi\nu_{\mathbf{t,ef}}t}} \int_{-\infty}^{0} \exp\Big(-\frac{(s-(\Delta_0 - v_{\mathbf{ter}}t))^2}{4\nu_{\mathbf{t,ef}}t}\Big)\,ds = \\ &\exp\Big(\frac{v_{\mathbf{ter}}^2 t}{4\nu_{\mathbf{t,ef}}} - \frac{v_{\mathbf{ter}}\Delta_0}{2\nu_{\mathbf{t,ef}}}\Big)\cdot\frac{1}{2}\Big(1+\operatorname{erf}\Big(\frac{v_{\mathbf{ter}}t - \Delta_0}{2\sqrt{\nu_{\mathbf{t,ef}}t}}\Big)\Big). \end{aligned} \tag{C9}$$

Therefore, $\varphi(z,t)$ is obtained as $\varphi(z,t) = I_1 + I_2$, and recovering $\hat{v}_s$ using (C1), gives:

$$\hat{v}_s(z,t) \;=\; v_{\mathbf{ter}}\,\frac{\big(1+\operatorname{erf}(p_0)\big)\,p_2}{\big(1+\operatorname{erf}(p_0)\big)\,p_2 + \big(1+\operatorname{erf}(p_1)\big)} \tag{C10}$$

855 where:

$$p_0 := \frac{v_{\mathbf{ter}}t - \Delta_0}{2\sqrt{\nu_{\mathbf{t,ef}}t}}, \qquad p_1 := \frac{\Delta_0}{2\sqrt{\nu_{\mathbf{t,ef}}t}}, \qquad p_2 := \exp\Big(\frac{v_{\mathbf{ter}}^2 t}{4\nu_{\mathbf{t,ef}}} - \frac{v_{\mathbf{ter}}\Delta_0}{2\nu_{\mathbf{t,ef}}}\Big). \tag{C11}$$

The above equation can be also written in a more compact form by using the identity $(1+\operatorname{erf}(\xi)) = \operatorname{erfc}(-\xi)$.

https://doi.org/10.5194/jecats-2026-12
Preprint. Discussion started: 28 July 2026

Appendix D: Terminal Velocity, $v_{\mathbf{ter}}$

We present the method used to compute the terminal velocity $v_{\mathbf{ter}}$ of randomly oriented spheroidal ice particles in a quiescent fluid under gravity, using the drag model by Ganser (1993). Recall that for spheroids $\mathcal{V} = \frac{4}{3}\pi a^3 \phi$, where a is the equatorial semi-axis and $\phi = c/a$ the aspect ratio. The Ganser model requires the following geometrical definitions: the volume-equivalent diameter $d_v = \left(6\mathcal{V}/\pi\right)^{1/3} = a\,(8\phi)^{1/3}$, and sphericity $\Psi = \pi d_v^2/S$ with S being the total surface area of the spheroid, computed as 1) Oblate ($\phi < 1$, $e = \sqrt{1-\phi^2}$): $S = 2\pi a^2\left[1 + \frac{1-e^2}{e}\tanh^{-1}(e)\right]$, 2) Prolate ($\phi > 1$, $e = \sqrt{1-\phi^{-2}}$): $S = 2\pi a^2\left[1 + \frac{\phi}{e}\sin^{-1}(e)\right]$, and 3) Sphere ($\phi = 1$): $S = 4\pi a^2$.

In addition, Ganser defines d_n as the diameter of a sphere whose projected area normal to the motion equals that of the spheroid: thus one writes $A_{\text{proj}} = \pi d_n^2/4$, and since the orientation-averaged projected area satisfies $\langle A_{\text{proj}}\rangle = S/4$ by Cauchy's theorem, one has $d_n = \sqrt{4\,\langle A_{\text{proj}}\rangle/\pi} = d_s$, where d_s satisfies $S = \pi d_s^2\,(\Rightarrow d_s = \sqrt{S/\pi})$.

Stokes' shape factor (unbounded fluid) is $K_1 = \frac{1}{3}(d_n/d_v) + \frac{2}{3}(d_s/d_v)$, and the generalized Reynolds number is $Re^* = Re\,K_1\,K_2$ with $Re = \frac{\rho_f v_{\mathbf{ter}} d_v}{\mu_{\text{ef}}}$, where μ_{ef} is the effective dynamic viscosity.

Newton's shape factor is fitted as $K_2 = 10^{1.8148(-\log_{10}\Psi)^{0.5743}}$.

With these, Ganser's drag model is given by:

$$C_D = \frac{24}{Re^*}\left(1 + 0.1118\,(Re^*)^{0.6567}\right)K_2 + \frac{0.4305\,K_2}{1 + 3305/Re^*}. \tag{D1}$$

To determine the terminal velocity, we write:

$$\tfrac{1}{2}\rho_f v_{ter}^2 C_D \langle A_{\text{proj}}\rangle = (\rho_p - \rho_f)\mathcal{V}g. \tag{D2}$$

Let $B = \frac{4(\rho_p-\rho_f)\rho_f g d_v^3}{3\mu_{\text{ef}}^2}$, where $\mu_{\text{ef}} = \frac{\mu}{C(r_{\text{eff}})}$ with $C(r_{\text{eff}})$ being the Cunningham correction factor accounting for slip effects at very small particle sizes (equivalent to non-continuum effects at high Knudsen numbers).

The Cunningham correction factor $C(a^*)$ is defined as:

$$C(r_{\text{eff}}) = 1 + \frac{\gamma}{r_{\text{eff}}}\left(1.257 + 0.400\,e^{-1.1\,\frac{r_{\text{eff}}}{\gamma}}\right). \tag{D3}$$

where γ is the mean free path and r_{eff} is the particle's effective radius defined as $r_{\text{eff}} = a\,\phi^{1/3}$.

Substituting $v_{\mathbf{ter}} = \frac{Re\,\mu_{\text{ef}}}{\rho_f d_v}$, gives the following implicit equation:

$$Re^2\,C_D(Re^*) = B. \tag{D4}$$

which is solved numerically for Re. Therefore, the terminal velocity is retrieved as:

$$v_{\mathbf{ter}} = \frac{Re\,\mu_{ef}}{\rho_f d_v}. \tag{D5}$$

https://doi.org/10.5194/jecats-2026-12
Preprint. Discussion started: 28 July 2026

Notably, because $\langle A_{\text{proj}} \rangle$ is the orientation-averaged projected area, Ganser's drag model inherently accounts for random tumbling orientation.

Appendix E: Inherent Growth Factor Γ^*

It should be emphasized that the current habit-dynamics framework does not represent bullet-rosette geometries, internal hollowing/branching morphologies, or ventilation effect.

To elaborate, incorporation of hollowing and branching together with habit-dependent ventilation is conceptually straightforward and can be implemented using well-documented microphysical relations Welss et al. (2024); doing so does not invalidate the terminal-velocity formulations for generalized spheroidal particles (for example, the Ganser-type parameterizations employed in this study Ganser (1993)) because those relationships remain applicable to the modified bulk shape and density descriptions.

By contrast, explicit treatment of bullet-rosette crystals poses practical difficulties. These habits typically develop after prolonged exposure to large ice supersaturations and therefore are likely less relevant to contrails. Specifically, in expanding contrails, the local relative humidity often relaxes to ice saturation level for a considerable period of time, and the subsequent recovery toward ambient humidity can be slow. Such a thermodynamic history does not generally provide the sustained, extreme supersaturation episodes necessary for bullet-rosette formation. Moreover, in-situ studies of contrail and contrail-cirrus microphysics usually report that plate- and column-like morphologies are observed more frequently than bullet-rosettes. Finally, parameterizations of the aerodynamic properties of complex rosette aggregates—especially broadly applicable terminal-velocity formulations—are scarce and poorly constrained, which further complicates their reliable inclusion in a habit-dynamics model.

For these reasons — and in order to introduce a state-of-the-art baseline for habit dynamics in contrail microphysics — we omit bullet-rosettes, hollowing/branching, and ventilation effects in the present work and reserve them for future extension and validation.

The available mathematical frameworks for habit dynamics are those by Chen and Lamb (1994) (based on the aspect-ratio hypothesis, defining $\frac{dc}{da} = \frac{\alpha_c}{\alpha_a}\frac{c}{a} := \Gamma\,\phi$) and Nelson and Baker (1996) (based on the facet hypothesis, defining $\frac{dc}{da} = \frac{\alpha_c}{\alpha_a} := \Gamma$), where α_a and α_c are the deposition coefficients of the basal and prism axes, respectively, a is half the basal-plane maximum width (equatorial radius), c is half the prism-plane height (transverse radius), and Γ is known as the Inherent Growth Factor (IGF). It is straightforward to show that the above dynamics are equivalent to (Harrington et al. (2019)):

$$\frac{d\phi}{d\mathcal{V}} = \frac{\Gamma^* - 1}{\Gamma^* + 2}\frac{\phi}{\mathcal{V}}, \tag{E1}$$

where $\Gamma^* = \Gamma$ in the Chen and Lamb model, and $\Gamma^* = \frac{\Gamma}{\phi}$ in the Nelson and Baker model.

https://doi.org/10.5194/jecats-2026-12
Preprint. Discussion started: 28 July 2026

Here, we should also highlight that the mathematical derivation of the above differential equation is general and does not include assumptions regarding temperature ranges or mixed-phase cloud regimes (where tiny supercooled water droplets and ice crystals coexist) Harrington et al. (2019). Therefore, the framework is also valid for contrail crystals, provided that the IGF factor is properly estimated or tuned. Diagnostic approaches to habit classification have also been proposed in the literature (e.g., Heymsfield et al. (2002)). However, a limitation of such diagnostic approaches is that temporal variations caused by local temperature and supersaturation changes may not be captured by static relations (Welss et al. (2024)). Another important point is that the well-known Schmidt–Appleman criterion sets the threshold for contrail formation, and the temperature required for contrail formation typically lies between approximately -35 and $-40\,^{\circ}\mathrm{C}$ (Li et al. (2023)), which coincides with the ice-cloud regime. However, once contrail crystals are formed, they may be advected into a mixed-phase regime, altering the vapor-transfer pathways and further complicating habit microphysics. However, this possibility is not considered in the present work, based on the assumption that temperature variations over the course of the contrail lifetime may not be significant.

Reviewing the literature on habit dynamics, predicting the IGF factor remains an active area of research, and in general, the available data are sparse for $T < -30\,^{\circ}\mathrm{C}$. However, extrapolations and fits to the limited available data have already been pursued in the literature (see, for example, Harrington et al. (2019) and Harrington et al. (2021)). To date, however, most IGF estimations rely on partially empirical or ad hoc closure assumptions.

In the present work, the IGF is formulated in a way to be consistent with the above state-of-the-art habit-dynamics models describing transitions between plate-like and columnar crystals, while remaining sufficiently simple to allow future extensions and refinement as controlled in-cloud observational data become available.

To this end, we set $\Gamma = \Gamma(T)$ for $T > -30\,^{\circ}\mathrm{C}$ and directly fit a function $\Gamma(T)$ to the available data in Chen and Lamb (1994); Zhang and Harrington (2014). However, for $T < -30\,^{\circ}\mathrm{C}$ we use Nelson and Baker model which directly accounts for dislocation growth and step nucleation theories, characterized by supersaturation immediately above the surface (i.e., surface supersaturation s_{surf}), a temperature-dependent characteristic supersaturation describing the supersaturation-dependence of surface-kinetic mediated growth (i.e., s_{char}), and the parameter N that describes the surface growth mode. An approximation for α that captures both dislocation growth and step nucleation theories was suggested by Nelson and Baker (1996):

$$\alpha(T, s_i) = \alpha_s \left(\frac{s_{\mathrm{surf}}}{s_{\mathrm{char}}}\right)^N \tanh\left(\frac{s_{\mathrm{char}}}{s_{\mathrm{surf}}}\right)^N \qquad \text{(E2)}$$

where α_s is the sticking probability/adsorption efficiency and is thought to be near unity Harrington et al. (2021); Laurencin et al. (2022). In addition, $N = 1$ is consistent with the dislocation growth whereas $N \geq 10$ is amenable to step nucleation.

Following Harrington et al. (2021), we compute s_{surf} as:

$$s_{\mathrm{surf}} \approx s_{\mathrm{diff}}^{1-\beta}\, s_{\mathrm{char}}^{\beta}. \qquad \text{(E3)}$$

https://doi.org/10.5194/jecats-2026-12
Preprint. Discussion started: 28 July 2026

with:

$$s_{\mathrm{diff,a}} = \frac{s_i}{1+L_a}, \quad L_a = \frac{a\,c\,\bar{v}_v}{4D_v C_\Delta(c,a)}, \quad s_{\mathrm{diff,c}} = \frac{s_i}{1+L_c}, \quad L_c = \frac{a^2\,\bar{v}_v}{4D_v C_\Delta(c,a)}. \tag{E4}$$

where D_v is the vapor diffusivity in air ($D_v = D_{v0}\left(\frac{T}{T_0}\right)^{1.94}\frac{p_0}{p}, D_{v0} = 2.11\times10^{-5}$ $\mathrm{m^2s^{-1}}$, $T_0 = 273.15$ K, $P_0 = 101325$ Pa), $\bar{v}_v$ is the mean speed of a vapor molecule ($\bar{v} = \sqrt{\frac{8k_BT}{\pi m_m}} = \sqrt{\frac{8RT}{\pi M}}$,), where k_B is Boltzmann's constant, m_m the mass of one molecule, R the universal gas constant and M the molar mass. Moreover, L_a, and L_c are unitless quantities that depend on the crystal geometry, and C_Δ is the capacitance Westbrook et al. (2008) evaluated one mean free path from the surface, i.e., $C_\Delta := C(a+\Delta, c+\Delta)$ where Δ is approximately the mean free path. In addition, β is a function of N which can be directly obtained from Harrington et al. (2021). Moreover, s_{diff}, is the surface supersaturation over the respective axis when the deposition coefficient is unity.

Notably, the Nelson and Baker formulation is expected to perform well at contrail-range temperatures and moderate supersaturation, but it falls short at low supersaturations Harrington et al. (2021, 2019). In this respect, it is suggested to account for residual errors by applying additional approximate parameterization techniques, more recently proposed in Harrington et al. (2021), to correct the surface supersaturation. However, the validity of such approximations has not yet been verified against experimental measurements (interested readers are referred to Pruppacher and Klett (1997); Harrington et al. (2021); Laurencin et al. (2022); Harrington et al. (2019); Harrington and Pokrifka (2024)).

From habit diagrams (e.g., Bailey and Hallett (2004); Bailey and Hallett (2010, 2009)), at temperatures colder than $-40,^\circ$C (contrail-range temperatures), there is a marked shift toward columnar behavior, except at low to moderate ice supersaturation (below $\approx 10\%$), where thick and irregular plates are observed. At moderate ice supersaturation (10%–25%), long solid columns and polycrystals with columnar and plate-like components are observed. Above approximately 25% ice supersaturation, bullet rosettes, long columns, and column-containing polycrystals are observed, with the frequency of bullet rosettes and columns increasing as ice supersaturation increases.

Therefore, for simplicity, consistency with the Nelson and Baker model, and correction of the low-supersaturation limit directly following the habit diagrams–while also explicitly addressing the frequently observed plate-like crystals in persistent contrails–we propose a small modification that corrects only the low-supersaturation shortcoming of the Nelson and Baker model by allowing plate-like crystals to reach a minimum of $\Gamma = 0.2$, corresponding to thick-plate habits.

Here, we introduce an ad hoc modification to the habit model to account exclusively for the lower supersaturation range (mimicking the 2D-nucleation–limited growth Zhang and Harrington (2014); Kuroda and Lacmann (1982)). The characteristic surface supersaturation $s_{\mathrm{char}} = s_{\mathrm{char}}(T)$ is specified using the Nelson–Baker/Harrington parameterization Harrington et al. (2021) and fitting smooth functions to the available experimental range and extrapolating these fits for lower temperatures.

We also point out that extrapolating the available data to cover a wider range, down to $-70,^\circ$C, does not change the structure of the characteristic supersaturation, as long as the monotonic trend documented in the literature is

https://doi.org/10.5194/jecats-2026-12
Preprint. Discussion started: 28 July 2026

preserved. However, the choice of extrapolation function primarily affects the upper-bound extent of the columnar crystals.

On choosing a critical supersaturation parameter $s_{\mathrm{cr.}}$, and a corresponding $\Gamma_{\mathrm{cr.}}$, the final form of the IGF for $T < -30\,^\circ\mathrm{C}$ is considered as:

$$\Gamma(T,s_i) = \Gamma_{\mathrm{cr.}} + \left(\frac{\alpha_c}{\alpha_a} - \Gamma_{\mathrm{cr.}}\right) e^{-\left(\frac{s_{\mathrm{cr.}}}{s_i}\right)^n}. \tag{E5}$$

where α_a, and α_c are obtained from Eq. (E2).

Based on the foregoing discussion, we adopt the parameter ranges $2\% < s_{\mathrm{cr}} < 5\%$, $\Gamma_{\mathrm{cr}} \in [0.05, 0.2]$, and $n \in [2,4]$. Numerical simulations show that, over these ranges, the model output exhibits at most moderate sensitivity to s_{cr}, negligible sensitivity to n, and negligible-to-moderate sensitivity to Γ_{cr}.

In this study, we have set $\Gamma_{\mathrm{cr.}} = 0.05$, $s_{\mathrm{cr.}} = 5\%$, and $n = 2$.

Further tuning of the model in the contrail regime should address a more general parameterization of low supersaturation and different types of monotonic extrapolation functions for the characteristic supersaturations. Such additional tuning or modification would mainly control the minimum and maximum bounds of ϕ.

Appendix F: Vapor Deposition Volumetric Growth Rate $f_{\mathcal{V}}$

The volumetric growth rate $f_{\mathcal{V}}$ is computed from a standard diffusion-limited growth model with latent-heat (thermal-resistance) coupling:

$$f_{\mathcal{V}} = \frac{4\pi C\, s_i}{\rho_{\mathrm{dep}}\left(\dfrac{R_v T}{e_i D_v'} + \dfrac{L_s}{k_{\mathrm{air}}' T}\left(\dfrac{L_s}{R_v T} - 1\right)\right)}. \tag{F1}$$

where $e_i = e_i(T)$ denotes the saturation vapor pressure over ice, and L_s is the latent heat of sublimation. Empirical formulas from Murphy and Koop (2005) are used to evaluate e_i and L_s. In addition, R_v represents the specific gas constant for water vapor, with a value of approximately 461.5 $\mathrm{J\,kg^{-1}\,K^{-1}}$. In the absence of hollowing and branching processes, the deposition density ρ_{dep} is approximated by the ice density, i.e., $\rho_{\mathrm{dep}} \approx \rho_{\mathrm{ice}} \approx 917$ kg m^{-3}. Moreover, D_v' denotes the kinetically limited vapor diffusivity, and k_{air}' the kinetically limited thermal conductivity, expressed as Zhang and Harrington (2014):

$$D_v' = \frac{2}{3}\frac{D_v}{A + B_d} + \frac{1}{3}\frac{D_v}{A + C_d}, \qquad k_{\mathrm{air}}' = \frac{2}{3}\frac{k_{\mathrm{air}}}{A + B_k} + \frac{1}{3}\frac{k_{\mathrm{air}}}{A + C_k}. \tag{F2}$$

where:

$$A = \frac{C}{C_\Delta}, \quad B_d = \frac{4 D_v C}{\alpha_a v_v a^2 \phi}, \quad C_d = \frac{4 D_v C}{\alpha_a \Gamma v_v a^2}, \quad B_k = \frac{4 k_{\mathrm{air}} C}{0.7\,\rho_{\mathrm{air}} c_p v_v a^2 \phi}, \quad C_k = \frac{4 k_{\mathrm{air}} C}{0.7\,\rho_{\mathrm{air}} c_p v_v a^2}. \tag{F3}$$

https://doi.org/10.5194/jecats-2026-12
Preprint. Discussion started: 28 July 2026

In above, k_{air} is the thermal conductivity of air (≈ 0.024 W m^{-1} K^{-1}), ρ_{air} is air density and c_p is the specific heat capacity of air (≈ 1005 J kg^{-1}K^{-1}). In addition, standard atmospheric relations are used to compute the air density, ρ_{air}, and pressure, P, from the temperature profile $T(z)$, where $T(z)$ follows the International Standard Atmosphere lapse rate -6.5×10^{-3} K m^{-1}.

Appendix G: Eulerian Equation for Supersaturation s_i

Ice supersaturation is defined as $s_i(\mathbf{x},t) \equiv \frac{q_v}{q_{vs}(T,p)} - 1$, so $q_v = q_{vs}(T,p)\,(1+s_i)$, where q_v is the water-vapour mixing ratio, $q_{vs}(T,p) = \dfrac{\varepsilon e_{si}(T)}{p - e_{si}(T)}$ the saturation mixing ratio over ice (with $\varepsilon = R_d/R_v$), c_N the ice number concentration, $\dot{m}$ the single-particle mass growth rate, and the volumetric deposition rate $S_{\text{dep}} = c_N\dot{m}$.

For compactness below we write $q_s \equiv q_{vs}(T,p)$ (so $q_v = q_s(1+s_i)$). We start from the vapour conservation equation with advection, an explicit deposition sink, and a general entrainment (mixing) operator $\mathcal{E}[q_v]$ which represents the net tendency of ambient vapour to be mixed into the plume:

$$\frac{Dq_v}{Dt} = -\frac{S_{\text{dep}}}{\rho_{\text{air}}} + \mathcal{E}[q_v]. \tag{G1}$$

Taking the material derivative of $q_v = q_s(1+s_i)$ gives

$$\frac{Dq_v}{Dt} = q_s\frac{Ds_i}{Dt} + (1+s_i)\frac{Dq_s}{Dt}. \tag{G2}$$

Equating the material form of (G1) with (G2) and solving for Ds_i/Dt yields the exact Eulerian evolution equation:

$$\frac{Ds_i}{Dt} = -\frac{1}{q_s}\frac{S_{\text{dep}}}{\rho_{\text{air}}} - \frac{1+s_i}{q_s}\frac{Dq_s}{Dt} + \frac{1}{q_s}\mathcal{E}[q_v]. \tag{G3}$$

A commonly used closure for the entrainment operator is the bulk relaxation form:

$$\mathcal{E}[q_v] = \frac{q_{\text{env}} - q_v}{\tau_{\text{entrain}}}, \tag{G4}$$

where $q_{\text{env}}(\mathbf{x},t)$ is the ambient vapour mixing ratio sampled at the plume/element location and τ_{entrain} is the entrainment timescale. Substituting (G4) into (G3) and using $q_v = q_s(1+s_i)$ gives

$$\frac{Ds_i}{Dt} = -\frac{1}{q_s}\frac{S_{\text{dep}}}{\rho_{\text{air}}} - \frac{1+s_i}{q_s}\frac{Dq_s}{Dt} + \frac{1}{q_s}\frac{q_{\text{env}} - q_s(1+s_i)}{\tau_{\text{entrain}}}. \tag{G5}$$

Noting that

$$\frac{q_{\text{env}} - q_s(1+s_i)}{q_s} = \frac{q_{\text{env}}}{q_s} - 1 - s_i \equiv s_{\text{env}} - s_i, \qquad s_{\text{env}} \equiv \frac{q_{\text{env}}}{q_s} - 1,$$

https://doi.org/10.5194/jecats-2026-12
Preprint. Discussion started: 28 July 2026

the entrainment contribution reduces to:

$$\frac{Ds_i}{Dt} = -\frac{1}{q_s}\frac{S_{\text{dep}}}{\rho_{\text{air}}} - \frac{1+s_i}{q_s}\frac{Dq_s}{Dt} + \frac{s_{\text{env}} - s_i}{\tau_{\text{entrain}}}\,. \tag{G6}$$

To obtain τ_{entrain}, we consider a Lagrangian plume element of mass M that entrains ΔM during Δt. The post-mix vapour is Schumann (2012):

$$q_v(t+\Delta t) = \frac{M\,q_v(t) + \Delta M\,q_{\text{env}}}{M+\Delta M} \qquad \Rightarrow \Delta q_v = \frac{\Delta M}{M+\Delta M}\,(q_{\text{env}} - q_v). \tag{G7}$$

Dividing by Δt and taking $\Delta t \to 0$ (to first order $\Delta M/(M+\Delta M) \approx \Delta M/M$) yields:

$$\frac{dq_v}{dt} = \frac{1}{M}\frac{dM}{dt}\,(q_{\text{env}} - q_v). \tag{G8}$$

Comparing with (G4) shows that the appropriate entrainment timescale is $\tau_{\text{entrain}} = \frac{M}{dM/dt}$.

Notably, τ_{entrain} can be simply parameterized using Gaussian or cylindrical plume element segment hypothesis. In the present research, we have assumed a locally constant pressure and temperature, and used cylindrical plume element segment hypothesis Schumann (2012).

Appendix H: The effect of wind shear

Vertical wind shear produces height-dependent horizontal advection that tilts and laterally displaces the contrail cross-section. Under the present separation ansatz the simplest consistent treatment is a kinematic remapping: a mass-conserving, levelwise horizontal translation of tracers that reproduces geometric distortion but does not feedback on local thermodynamic or microphysical state. Full two-way coupling requires abandoning the separation ansatz and solving the 3-D coupled system. As a low-cost, physically interpretable intermediate, one may instead add an implicitly treated, localized relaxation (entrainment) term to the prognostic ice-supersaturation equation, weighted by a plume-fraction or concentration indicator, which mixes ambient and plume air at the tilted edges, thereby producing first-order feedback of shear on microphysics while remaining operator-split and computationally inexpensive.

Nevertheless, in this research, the effect of vertical wind shear is incorporated by linearizing the horizontal wind field about a reference height z_{ref}:

$$u(z) = u(z_{\text{ref}}) + S_x\,(z - z_{\text{ref}}), \qquad v(z) = v(z_{\text{ref}}) + S_y\,(z - z_{\text{ref}}), \tag{H1}$$

where u and v denote the streamwise (x) and cross-stream (y) wind components, respectively, and $S_x = \partial u/\partial z$ and $S_y = \partial v/\partial z$ are the corresponding vertical shear rates.

https://doi.org/10.5194/jecats-2026-12
Preprint. Discussion started: 28 July 2026

Separating the mean advection from the shear-induced contribution, the differential horizontal velocities experienced by a parcel at height $z(t)$ are:

$$\delta u(z,t) = S_x\left(z(t) - z_{\mathrm{ref}}\right), \qquad \delta v(z,t) = S_y\left(z(t) - z_{\mathrm{ref}}\right). \tag{H2}$$

The cumulative lateral displacement due to shear over the time interval $[t_0, t_1]$ is then given by:

$$\Delta x = S_x \int_{t_0}^{t_1} \left(z(t) - z_{\mathrm{ref}}\right) \mathrm{d}t, \qquad \Delta y = S_y \int_{t_0}^{t_1} \left(z(t) - z_{\mathrm{ref}}\right) \mathrm{d}t. \tag{H3}$$

In practice, these integrals are evaluated numerically using a discrete representation of the vertical trajectory and a trapezoidal quadrature.

Vertical parcel motion is modeled using the following equation,

$$\frac{\mathrm{d}z}{\mathrm{d}t} = -v_s(z,t). \tag{H4}$$

The resulting discrete vertical positions $z(t_n)$ are used to evaluate the shear-induced displacements Δx and Δy.

Table H1. CoCiP specifications used for comparison

Parameter	**Value (actual)**	**Units**
nvpm_ei_n	1×10^{14}	particles kg^{-1} fuel
nvpm_ei_n enhancement factor	1.0	(dimensionless)
fuel_flow	1.0	kg s^{-1}
true airspeed	240.0	m s^{-1}
aircraft type	B738	-
engine UID	`CFM56-7B`	-
number of engines	2	-
aircraft mass	60000.0	kg
wingspan	34.32	m
engine efficiency	0.295	(dimensionless)
flight altitude	11000	m
vertical shear (shear variable)	-1.0×10^{-3}	s^{-1}
wind field	0 (all levels)	m s^{-1}
temperature (MET field)	212.0	K
lon/lat center	$(0.1°,\ 50.0°)$	degrees
RHi	$\begin{cases} 1.15 & 10800 \le z < 11200 \\ 0.85 & \textbf{elsewhere} \end{cases}$	-